



**HAL**  
open science

## Correlation of multi-temporal ground-based optical images for landslide monitoring

Julien Travelletti, Christophe Delacourt, Pascal Allemand, Jean-Philippe Malet, Jean Schmittbuhl, Renaud Toussaint, M. Bastard

► **To cite this version:**

Julien Travelletti, Christophe Delacourt, Pascal Allemand, Jean-Philippe Malet, Jean Schmittbuhl, et al.. Correlation of multi-temporal ground-based optical images for landslide monitoring. ISPRS Journal of Photogrammetry and Remote Sensing, 2012, 70, pp.39-55. 10.1016/j.isprsjprs.2012.03.007 . insu-00694179

**HAL Id: insu-00694179**

**<https://insu.hal.science/insu-00694179>**

Submitted on 15 May 2019

**HAL** is a multi-disciplinary open access archive for the deposit and dissemination of scientific research documents, whether they are published or not. The documents may come from teaching and research institutions in France or abroad, or from public or private research centers.

L'archive ouverte pluridisciplinaire **HAL**, est destinée au dépôt et à la diffusion de documents scientifiques de niveau recherche, publiés ou non, émanant des établissements d'enseignement et de recherche français ou étrangers, des laboratoires publics ou privés.

Elsevier Editorial System(tm) for ISPRS Journal of Photogrammetry and Remote  
Sensing  
Manuscript Draft

Manuscript Number:

Title: Correlation of multi-temporal ground-based images for landslide monitoring: application, potential and limitations.

Article Type: Full Article

Keywords: image cross-correlation; image matching; landslide; time-lapse photography; displacement monitoring

Corresponding Author: Dr. Jean-Philippe Malet,

Corresponding Author's Institution: CNRS / IPGS

First Author: Julien Travelletti

Order of Authors: Julien Travelletti; Christophe Delacourt; Pascal Allemand; Jean-Philippe Malet; Jean Schmittbuhl; Renaud Toussaint; Mickael Bastard

# 1 **Correlation of multi-temporal ground-based images for** 2 **landslide monitoring: application, potential and limitations.**

3

4 Travelletti J. (1,2), Delacourt C. (3), Allemand P. (4), Malet J.-P. (1), Schmittbuhl J. (1),  
5 Toussaint R. (1), Bastard M. (1)

6

7 (1) Institut de Physique du Globe de Strasbourg, CNRS UMR 7516, Université de Strasbourg /  
8 EOST, 5 rue René Descartes, 67084 Strasbourg Cedex, France. E-mail:  
9 julien.travelletti@unistra.fr

10 (2) GEOPHEN - LETG, CNRS UMR 6554, Université de Caen Basse-Normandie, Caen, France

11 (3) Institut Universitaire Européen de la Mer, CNRS UMR 6538, Université Européenne de  
12 Bretagne, Brest, France.

13 (4) Laboratoire des Sciences de la Terre, CNRS UMR 5570, Université de Lyon & Ecole  
14 Normale Supérieure, Lyon, France.

15

## 16 **Abstract**

17 The objective of this work is to present a low-cost methodology to monitor the displacement of  
18 continuously active landslides from ground-based optical images analyzed with a normalized  
19 Image Correlation technique. The performance of the method is evaluated on a series of images  
20 acquired on the Super-Sauze landslide (South French Alps) over the period 2008-2009. The  
21 image monitoring system consists in a high resolution optical camera installed on a concrete pillar  
22 located on a stable crest in front of the landslide and controlled by a datalogger. The data are  
23 processed with a cross-correlation algorithm applied on the full resolution images in the  
24 acquisition geometry. Then, the calculated 2D displacement field is ortho-rectified with a back  
25 projection technique using a high resolution DEM interpolated from Airborne Laser Scanning  
26 (ALS) data. The heterogeneous displacement field of the landslide is thus characterized in time  
27 and space. The performance of the technique is assessed using as reference differential GPS  
28 surveys of a series of benchmarks. The sources of error affecting the results are then discussed.  
29 The strongest limitations for the application of the technique are related to the meteorological,  
30 illumination and ground surface conditions inducing partial or complete loss of coherence among  
31 the images. Small changes in the camera orientation and the use of a mono-temporal DEM are the  
32 most important factors affecting the accuracy of the ortho-rectification of the displacement field.

33 Because the proposed methodology can be routinely and automatically applied, it offers  
34 promising perspectives for operational applications like, for instance, in early warning systems.

35

36 **Keywords:** image cross-correlation; image matching; landslide; time-lapse photography;  
37 displacement monitoring

38

## 39 **1 Introduction**

40 Displacement monitoring of unstable slopes is a crucial tool for the prevention of hazards. It is  
41 often the only solution for the survey and the early-warning of large landslides that cannot be  
42 stabilized or that may accelerate suddenly and potentially fluidize in highly mobile mudflows.  
43 The choice of an adequate monitoring system depends on the type and size of landslide, the range  
44 of observed velocity, the required frequency of acquisition, the desired accuracy and the financial  
45 constraints. Displacement monitoring techniques applied on landslides can be broadly subdivided  
46 in two main groups: geodetic and remote-sensing techniques.

47 Geodetic surveying consist in detecting geometrical changes in the landslide topography by  
48 measuring geometric parameters such as angles, distances or differences in elevation (e.g.  
49 levelling, tacheometry; Meissl & Naterop, 1995). These techniques necessitate the installation of  
50 benchmarks or targets in and outside the landslide and in measuring their position at different  
51 times. They have the advantage to be very accurate (0.2 to 2.0 cm) with a high potential of  
52 automation (Malet et al., 2002; Jaboyedoff et al., 2004; Foppe et al., 2006). Furthermore, many  
53 authors demonstrated the efficiency of permanent (Malet et al., 2002) and non-permanent  
54 (Squarzoni et al., 2005; Brunner et al., 2007) differential Global Positioning System (dGPS) for  
55 landslide monitoring with a centimetric accuracy during any daytime and weather conditions.  
56 However, because landslides can show highly variable displacement rates in time and space  
57 according to the local slope conditions (bedrock geometry, distribution of pore water pressures),  
58 the major drawbacks of the geodetic techniques are (1) to provide only discrete point  
59 measurements of the displacement and (2) the costs of installation and maintenance of the survey  
60 network. They are usually only justified in the case of a real risk for the population.

61 Remote-sensing techniques appear to be an interesting and complementary tool to obtain  
62 spatially-distributed information on the kinematics (Delacourt et al., 2007) which is also justified  
63 by the need to investigate landslides from safe and remote places because of the inaccessibility of  
64 mountainous terrains. Remote-sensing techniques give the possibility to discriminate stable and  
65 unstable areas and to map sectors within the landslide with different kinematics from a regional to

66 a local scale. They are also useful tools for a process-based analysis of the deformation field  
67 affecting the slope (Casson et al., 2005; Teza et al., 2008; Oppikofer et al., 2008). Remote-  
68 sensing techniques can be operational from spaceborne, airborne and ground-based platforms. In  
69 the last decades, the development of ground-based platforms for landslide monitoring at the local  
70 scale provided many advantages over spaceborne and airborne platforms despite a shorter spatial  
71 coverage (Corsini et al., 2006). The geometry and frequency of acquisitions are more flexible and  
72 adaptable to any type of local environment. Furthermore, the installation of the monitoring system  
73 is generally relatively easy. In addition ground-based platforms are permanent installations that  
74 allow a continuous monitoring (Casagli et al., 2004; Delacourt et al., 2007). Three main  
75 categories of ground-based remote sensing techniques are used in landslide monitoring: Ground-  
76 Based Synthetic Aperture Radar Interferometry (GB-InSAR), Terrestrial Laser Scanning (TLS)  
77 and Terrestrial Optical Photogrammetry (TOP). A non exhaustive review of the main advantages  
78 and disadvantages of these techniques is presented in Table 1. Detailed reviews of the application  
79 of GB-InSAR and TLS to landslides can be found in Luzi (2010), Corsini et al. (2006),  
80 Tarchi et al. (2003), Jaboyedoff et al. (2010), Teza et al. (2007, 2008) and Monserrat & Crosetto  
81 (2008). A state-of-the art of the application of TOP to landslide and related geomorphologicla  
82 processes is given below.

83 TOP is a very cost-effective technique with implementation, operating and equipment costs much  
84 lower than GB-InSAR and TLS. The technique consists in acquiring digital optical images  
85 represented using a matrix of intensity values (brightness) recorded at each pixel of the Charge  
86 Coupled Device (CCD) of the camera. While aerial images are acquired on overhead photographs  
87 from an aircraft, TOP uses RGB images acquired from a spot very close to the ground (Jiang et  
88 al., 2008). In the last decades, camera self-calibration and analytical processing techniques allow  
89 the use of non-metric cameras and of simplified camera calibration algorithms to compute digital  
90 elevation models using the principle of stereoscopic views (Mikhail et al., 2001; Jiang et al.,  
91 2008). In the current state, the application of terrestrial images for landslide monitoring is mostly  
92 related to the production of DEMs for image ortho-rectification and sediment budget analysis  
93 (Bitelli et al., 2004, Pesci et al., 2004; Cardenal et al., 2008), and more recently to the  
94 characterization of the slope morpho-structure (Lim et al., 2005; Sturzenegger & Stead, 2009).

95 Using correlation techniques, two-dimensional displacement fields can be derived by tracking  
96 objects in two images acquired at different time. So far, image correlation techniques have been  
97 applied only on aerial and satellite images (e.g. SPOT, QuickBird, OrbView, EROS) for the  
98 creation of landslide displacement maps (Casson et al., 2003; Delacourt et al., 2004; LePrince et  
99 al., 2008); the use of image correlation on terrestrial images has not been as popular for

100 permanent landslide monitoring as in other application field such as in solid and fluid mechanics  
101 for the characterization of the deformation pattern of soil/rock samples (White et al., 2003;  
102 Chambon et al., 2003; Küntz et al., 2005) or for the monitoring of other natural processes such as  
103 ice glaciers (Corripio et al., 2004; Fallourd et al., 2010; Maas et al., 2008) or volcanoes (Honda &  
104 Nagai, 2002). Only Delacourt et al. (2007) demonstrated an efficient application of TOP for  
105 landslide monitoring which consisted in the determination of the landslide boundaries and in the  
106 qualitative estimation of the spatial variability of displacement at the La Clapière landslide  
107 (French Alps) with an image acquisition system installed at 1 km-distance.  
108 Generally, the 2D displacements (in pixel) evaluated by the correlation algorithm have an  
109 accuracy of about 0.2 pixel (Casson et al., 2005; Delacourt et al., 2007) in the image plane,  
110 corresponding to an accuracy of millimeters to several centimeters for distances of about 100 m in  
111 the local coordinate system (Kraus & Waldhäusl, 1994).  
112 The major sources of errors affecting the displacement calculations and thus potentially limiting  
113 the efficiency of TOP for an operational landslide monitoring can be classified in two groups:  
114 (i) the parameters affecting the Image Correlation computation and (ii) the external parameters  
115 influencing the ortho-rectification procedure.  
116 The objective of this work is therefore to evaluate the potential and the limitations of TOP for the  
117 permanent monitoring of landslide using Image Correlation (IC) techniques. The dataset of  
118 images available for the Super-Sauze landslide (South French Alps) for the period 2008-2009 is  
119 used. First, the steps in the data acquisition and data processing (image correlation, ortho-  
120 rectification) are presented and the results are evaluated using the displacement of benchmark  
121 measured by DGPS. Second, the main advantages and disadvantages of the method, and the  
122 influence of external factors on the precision and the accuracy of the results are discussed.  
123 Throughout this work, the accuracy is defined as the systematic difference between a measured  
124 quantity and the true value, and precision is defined as the random difference between multiple  
125 measurements of the same quantity.

126

## 127 **2 Experimental Site: the Super-Sauze landslide**

128 To evaluate the potential of correlation of ground-based images for landslide monitoring, the  
129 dataset available at the Super-Sauze landslide, triggered in the Callovo-Oxfordian black marls of  
130 the South French Alps (Alpes-de-Haute-Provence, France; Fig. 1A, 2A, B) is used. The landslide  
131 is located in the upper part of the Sauze torrential catchment. In the 1960s, the area was affected  
132 by rock failures in the scarp area. The failed material composed of rocky panels progressively

133 transformed into a silty-sandy matrix integrating marly fragments of heterogeneous sizes through  
134 successive weathering cycles (Malet et al., 2003). From the 1970s until today, the landslide  
135 material is gradually filling a torrential stream located downstream with a typical range of  
136 displacement rate between 1 to 3 cm.d<sup>-1</sup> on average and possible higher velocities up to 40 cm.d<sup>-1</sup>  
137 during acceleration periods (Malet et al., 2002). In 2007, the mudslide extent over a distance of  
138 920 m between an elevation of 1980 m at the scarp and 1760 m at the toe with an average width  
139 of 135 m and a average slope of 25°. The total volume is estimated at 560,000 m<sup>3</sup> (Travelletti &  
140 Malet, submitted).

141 The kinematics of the landslide is currently monitored by Differential Global Positioning System  
142 (DGPS) and Terrestrial Laser Scanning (TLS), and by a remote camera monitoring system. This  
143 instrumentation consists in a low-cost D70 Nikon non-metric reflex digital camera installed on a  
144 concrete pillar located on a stable crest in front of the landslide at a distance of 300 m from the  
145 lower part and 900 m from the main scarp (Fig. 1A, B, C). The acquisition system is controlled  
146 by a datalogger (Campbell CR10) and the power is provided by a 40 W solar panel. The  
147 characteristics of the acquisition are presented in Table 2. Each four days, four images are  
148 acquired at 11:00, 12:00, 13:00 and 14:00 GMT in order to increase the probability of having at  
149 least one image with good meteorological conditions. Each photograph (6 Mb) is stored in a  
150 native file format to avoid any loss of information.

151

## 152 **3 Methodology**

153 The steps in the data processing workflow consist in (1) correlating the images by pairs in their  
154 original acquisition geometry to prevent any loss of information, and (2) ortho-rectifying the  
155 calculated displacement fields using a high-resolution digital elevation model interpolated from  
156 airborne LiDAR data. The daily images presenting the best ground texture contrast and the most  
157 homogeneous lightening are selected based on expert judgment. The detailed methodology is  
158 summarized in Fig. 3 and described below.

### 159 **3.1 Principle of the Image Correlation technique**

160 The 2D displacement field is obtained by correlating two optical images acquired at different  
161 time. The image correlation technique is based on the automatic identification of identical texture  
162 patterns within an image by maximizing a correlation function (Lewis, 1995; Baratoux et al.,  
163 2001; Debella-Gilo & Käab, 2010). Its principle adapted for landslide kinematics analysis is  
164 described in Delacourt et al. (2007). Visible ground features have to be superimposed on two

165 successive images on stable parts located outside the landslide. On the areas affected by landslide  
166 movements, the visible and recognizable features are shifted by the displacements. In order to  
167 quantify the ground displacements, a correlation window is defined on a reference (often the  
168 oldest) image. The corresponding window is searched in a pre-defined explored area belonging to  
169 the second image. The starting point of this explored area is the expected position of the window  
170 as if no displacement occurred between two acquisitions. The process is repeated for each pixel of  
171 the reference image. The Euclidean distance between the reference point and the matching point  
172 represents the displacement magnitudes in the image plane. By modifying the zone of interest, it  
173 is then possible to determine the displacements at various positions within the images (Fig. 4). It  
174 is important to note that the normalized cross-correlation technique cannot track objects that start  
175 to rotate significantly or are affected by important perspective distortions (Lewis, 1995).

176 The size of the correlation window is a compromise between the desired accuracy on the  
177 displacement estimates and the spatial resolution of the velocity field (Delacourt et al., 2007). An  
178 increase of the size of the correlation window ensures a good signal to noise ratio and thus a good  
179 precision, but the accuracy on the displacement estimates decreases because of their averaging on  
180 a larger correlation window. This compromise is difficult to find when some parts of the landslide  
181 are well defined in terms of ground texture while others parts are not. Hierarchical correlation  
182 techniques allow to overcome this problem by automatically changing the physical size of the  
183 correlation window and of the explored area during the correlation computations. The physical  
184 size is defined as the effective landslide surface covered by the correlation window (Rohaly,  
185 2002; Aloui & Ibn-Elhaj, 2009).

186 In this work, a sub-pixel hierarchical correlation technique is used (Chambon, 2003; Bastard,  
187 2009). The RGB images are first converted in gray-scale images on which a 3x3 pixel Sobel  
188 convolution matrix is applied to highlight the ground surface texture. The gradient values are then  
189 correlated (Chambon, 2003). Four successive degradations of the image resolution are applied  
190 following a pyramidal approach for changing the physical size of the correlation window and of  
191 the explored area by down-sampling the gradient values of the full resolution image (D'Antone,  
192 1995; Kumar & Banerjee, 1998) (Fig. 4). The optimum sizes of the correlation window (16x16  
193 pixels) and of the explored area (32x32 pixels) were identified with a trial and error procedure.  
194 These parameters are constant during the correlation computation. The correlation starts with the  
195 lowest resolution image in order to determine the largest displacements. Then the location of the  
196 pixel with the maximum cross-correlation value is used as the centre of the zone of interest for the  
197 next correlation step at a higher resolution. The spatial location of the maximum correlation value  
198 in the highest resolution image is thus progressively better estimated (Fig. 4). Ignoring high

199 resolution information at the first computational step decreases the probability to reach a local  
200 minima of the correlation function and, consequently, to obtain wrong matches in the  
201 correspondence solutions (Aloui & Ibn-Elhaj, 2009). In addition, this approach ensures a higher  
202 probability of reliable correlation peak detection (Anandan et al., 1993). The sub-pixel  
203 displacement is computed after the correlation at the highest resolution image. An iterative  
204 procedure is used to find the maxima of the correlation function interpolated with a bi-parabolic  
205 formula and with a maximization procedure based on the simplex method (Press et al., 1997;  
206 Chambon, 2003).

207 The correlation results consist in matrices of displacements  $\Delta u$  and  $\Delta v$  along the  $u$ - and  $v$ -axes in  
208 the image plane with their associated correlation index (Fig. 4). Because the pixel size is not  
209 constant in the image due to the oblique acquisition, the displacements field correlated in the  
210 image plane cannot be directly interpreted in terms of metric displacements. Therefore an ortho-  
211 rectification procedure is necessary for a quantitative analysis of the displacement fields.

### 212 **3.2 Ortho-rectification of the displacement field using high-resolution** 213 **digital elevation models (DEMs)**

214 The ortho-rectification procedure consists in transforming the central projection of the image into  
215 an orthogonal view of the ground by correcting the effects of various distortion sources such as  
216 camera orientation, topographic effects and lens characteristics (Kraus & Waldhäusel, 1998). In  
217 terrestrial photogrammetry, distortions induced by topography effects are the most important due  
218 to the oblique acquisition of the images. The ortho-rectification is used to convert the initial  $(u, v)$   
219 and the final  $(u+\Delta u, v+\Delta v)$  positions of the displacement vectors in a local coordinate system.  
220 The conversion is possible if a Digital Elevation Model (DEM) of the object is available in order  
221 to relate two-dimensional pixel positions in the image plane to three-dimensional points in a local  
222 coordinate system using parametric approaches (Hemmler & Wiedemann, 1997).

223 In our approach, the rotation angles defining the external orientation of the camera are first  
224 determined using the relationship between the image coordinates  $(u, v)$  and the local coordinates  
225 system  $(X, Y, Z)$  given by the collinearity equations. These equations are based on the principle that  
226 each point in the local coordinate system is projected with a straight line through the projection  
227 center (origin of the camera) into the image plane (Bonneval 1972, Kraus & Waldhäusel, 1994).  
228 Knowing the exact location of the camera and assuming that the principal point coordinates is at  
229 the center of the image, the external angle defining the absolute orientation of the camera in the  
230 local reference system can be determined with Ground Control Points (GCPs; Corripio, 2004).

231 In our case, the GCPs located on the landslide by DGPS measurements consisted in red-yellow  
232 squared metal targets with a dimension of 0.5x0.5 m identified both in the image plane and in the  
233 local coordinate system. A serie of 95 pairs of GCPs distributed on the image plane and in the  
234 local reference system were measured (Fig. 5). The centers of the GCPs are positioned in the  
235 local coordinate system with an average 3D accuracy of 0.02 m and a standard deviation of  
236 0.01 m. The coordinates  $(u,v)$  of the GCPs in the image plane are determined by manual picking  
237 with an estimated accuracy of about 2 pixels. Among the 95 GCPs, 45 are used to compute the  
238 external parameters and 40 are kept to calculate the accuracy of the transformation (section §  
239 5.2.1). A least mean square minimization technique based on Singular Value Decomposition  
240 (SVD) between observed and calculated GCPs in the image plane is used to determine the  
241 external parameters that satisfy the collinearity equations (Heikkilä & Silven, 1997).  
242 Then, a backward projection method is applied to allocate a 3D coordinate to each pixel  
243 coordinate in the image plane (Mikhail et al., 2001; Corripio, 2004). In the backward projection,  
244 instead of interpolating in the local reference system, the interpolation is carried out in the image  
245 geometry. A bilinear interpolation is used to associate the  $X,Y,Z$  coordinates for each initial point  
246  $(u,v)$  and each final point  $(u+\Delta u, v+\Delta v)$  in the image plane. Because the interpolation of the  $X,Y,Z$   
247 coordinates is carried out directly on a regular grid, this method is easier to implement than the  
248 classical forward method which projects the image location in the DEM geometry (Mikhail et al.,  
249 2001). Moreover, a forward projection would transform the pixel coordinates in the image plane  
250 to irregularly distributed points in the local reference system which are then interpolated into a  
251 regular grid. Therefore, each point of the DEM is projected in the image using the collinearity  
252 equations. Because stereoscopic pairs of images acquired simultaneously from two cameras at  
253 different view spots are not available because of the local site configuration, two Airborne Laser  
254 Scanning (ALS) dense point clouds acquired in October 2007 and July 2009 have been used to  
255 interpolate 0.25m mesh-size DEMs with a planar and elevation accuracy of 0.07 m. The  
256 displacement correlated during the year 2008 and 2009 were orthorectified using the DEMs of  
257 2007 and 2009 respectively In order to avoid the projection of duplicate points in the same  
258 position, the points of the DEMs visible from the camera viewpoint are identified by using the  
259 sightline method (Fisher, 1994; Franklin & Ray, 1994). The sightline is defined as the straight  
260 line going from the camera location to the position located in the gridded DEM. The visible  
261 points of the DEM of 2009 are presented in Fig 2B. About 57 % of the landslide area is visible  
262 from the camera view point, no displacements can be obviously measured in the invisible areas.  
263 The visible points of the DEM are then back-projected and linearly interpolated in the image  
264 plane. Three grids for the X, Y and Z coordinates (Fig. 3) are then obtained. The re-projection of

265 the displacement vector components in the local reference system is then straightforward, and the  
266 re-projected vector components are averaged and smoothed in a regular grid with a mesh size of  
267 1m.

268 The use of a mono-temporal DEM for the ortho-rectification of the displacements is a strong  
269 hypothesis that the global landslide morphology remains constant over the period and affect the  
270 accuracy of the conversion of the displacement vector in the local coordinate system. However, it  
271 will be further demonstrated that this method is still a relevant estimation for our purpose with  
272 reference to the amplitude of the observed displacements.

### 273 **3.3 Image resolution at the terrain surface**

274 The effective (e.g. ground) pixel size is calculated with the DEM of 2009 projected in the image  
275 geometry. The effective pixel size is one limiting parameter for the accuracy of the correlation.  
276 The pixel size depends on (1) the distance between the object and the camera (Fig. 6A) and  
277 (2) the angle of incidence which is defined as the complementary angle between the line of sight  
278 of the camera and the normal of the terrain surface (Fig. 6B). A low incidence angle means that  
279 the line of sight is nearly tangential to the topography. Consequently, the pixel projection in the  
280 local coordinate system is very close to an invisible zone from the camera view point.

281 The pixel size determines the minimum theoretical displacement that can be detected by the  
282 Image Correlation technique for a pixel-level correlation. Below this displacement threshold, the  
283 accuracy solely depends on accuracy of the sub-pixel correlation. Globally, the incidence angle  
284 on the landslide ranges from  $0^\circ$  to  $40^\circ$  and the pixel size varies from  $1 \cdot 10^{-2} \text{ m}^2$  in the lower part (at  
285 an average distance of 300m) to  $3 \cdot 10^{-2} \text{ m}^2$  in the upper part of the landslide (at an average  
286 distance of 900 m; Fig. 6A,B). The upper part is characterized with a pixel size often larger than  
287  $0.04 \text{ m}^2$ , especially in areas where the angle of incidence is less than  $5^\circ$ . Therefore the lowest  
288 accuracy is expected in this region because a small  $\Delta v$  and  $\Delta u$  displacement can lead to an  
289 important  $\Delta X$ ,  $\Delta Y$ ,  $\Delta Z$  metric displacement.

290 In order to better assess the effect of the image resolution on the displacement estimate, a rigid  
291 displacement of  $\Delta v=1$  pixel and  $\Delta u=1$  pixel is imposed for each  $(u,v)$  location in the image plane  
292 and then converted in the local reference system. The metric displacements plotted versus their  
293 corresponding angle of incidence and the histograms with the cumulative distribution function of  
294 the displacements are presented in Fig. 7. If only a pixel-level correlation technique is used, the  
295 calculated displacements correspond to the minimum displacements that can be detected along  
296 the  $u$ -axis and  $v$ -axis of the image. In areas where the incidence angle is less than  $5^\circ$ , the  
297 minimum displacement drastically increases to several meters for both directions (Fig. 7A, B).

298 Therefore no strong confidence is given to areas whose incidence angle is lower than  $5^\circ$ . 11% and  
299 2% of the pixels in the landslide area with an angle of incidence lower than  $5^\circ$  has a metric  
300 sensitivity to one pixel of displacement greater than 0.5 m in the  $v$ -axis and the  $u$ -axis (Fig. 7C,  
301 D). Globally, 50% of the pixels in the image plane inside the landslide area show a metric  
302 sensitivity less than 0.17 m for one pixel displacement along the  $v$ -axis and 0.07 m along the  $u$ -  
303 axis. Minimum displacements for a pixel-level correlation in respectively the  $u$  and  $v$ -direction  
304 are 0.04 m and 0.06 m in the lower part of the landslide and 0.09 m and 0.11 m in the upper part.

### 305 **3.4 Post-processing: displacements filtering**

306 Filtering criteria are necessary to remove the badly correlated points and improve the signal to  
307 noise ratio (Casson et al., 2003; Berthier et al., 2005; Wangenstein et al., 2006; Debella & Käab,  
308 2010). Three criteria are used in this study to filter aberrant displacements in the image plane  
309 coordinate system and in the local coordinate system. There are based on:

- 310 1. the value of the correlation peak coefficient: loss of coherence can occur during the  
311 correlation computations because change in surface states between a reference image and  
312 the correlated image are high, resulting thus in low correlation coefficients. Defining a  
313 threshold value has the consequence to increase the percentage of realistic displacements.  
314 A high threshold coefficient of  $r=0.6$  was selected to remove the badly correlated points.  
315 However, the correlation peak coefficient alone is not a sufficient discriminating criteria  
316 because some points can display a high correlation coefficient even if they do not  
317 represent the same object (e.g. two trees or large stones having the same geometry;  
318 Casson et al., 2005);
- 319 2. the value of displacement amplitudes and directions: points which detect an upslope  
320 displacement detection and a too important displacement amplitude with reference to  
321 prior knowledge on the landslide kinematics.
- 322 3. the displacements assigned to invisible areas from the camera viewpoint because of small  
323 ortho-rectification errors in the conversion to the local coordinate system.

324 Table 2 presents the results of the filtering on the total number of correlated points.  
325 Displacements correlated from images acquired in the summer season (23–27 July 2008) and in  
326 the autumn season (19–23 October 2008) highlight the differences in the number of remaining  
327 values for the two seasons. The amount of remaining point after filtering varies between 80% and  
328 90% in the summer period and can decrease to 50% in the autumn period. This is mainly  
329 explained by the different illumination conditions (low sun elevation) that affect the quality of the  
330 correlation. This aspect will be discussed further in section §6.1.3. The upper part of the landslide

331 is the most affected by the filtering criteria. This part generally shows a percentage of remaining  
332 values lower than in the middle and lower parts of the landslide. This is explained by the fact that  
333 the upper part has a more complex morphology. Consequently the effects of illumination changes  
334 are more important than in the middle and the lower parts, especially in autumn. In addition, the  
335 angle of incidence in this area can be low (5 to 10°) and thus sensitive to small displacements of  
336 the camera.

## 337 **4 Results**

### 338 **4.1 Displacement maps of the landslide**

339 A set of images over the period May–July 2008 is used to illustrate the potential of the technique  
340 for the characterization of the kinematics during an acceleration period triggered by high rainfall  
341 amounts and a fast melting of the snow cover.

342 Figure 8 shows an example of displacement rate (in  $\text{pixel.day}^{-1}$ ) of the ground surface in the  
343 image plane derived from image pairs of 20–28 May, 1–4 June and 9 June–13 June. The reference  
344 is the image of 20 May. The contrast in displacement rates between the landslide area and the  
345 stable area gives confidence on the calculated velocity field. One can notice that the pattern of  
346 displacement rate is heterogeneous spatially and temporarily. The upper part of the landslide  
347 displays the highest velocities ranging from 1 to 7  $\text{pixels.day}^{-1}$  while the lower part displays  
348 velocities of less than 4  $\text{pixels.day}^{-1}$ . No quantitative comparisons can be carried out at this stage  
349 because the pixel sizes vary strongly in the image (Fig. 6A). From the 20 May to the 13 June,  
350 cumulated displacements up to 110 pixels are observed in the upper part. The maximum of  
351 displacement rate is observed around the 1<sup>st</sup> June. Then the landslide decelerates to displacement  
352 rate of about 1  $\text{pixel.day}^{-1}$ .

353 Some local specific displacement patterns are also clearly highlighted; for instance, the presence  
354 of a stable *in-situ* crest located in the landslide body is perfectly identified in the correlated  
355 images.

356 Figure 9 presents the amplitude of the 3D ortho-rectified displacement rates for the period 1<sup>st</sup>  
357 June– 4<sup>th</sup> June in the local coordinate system. The difference of kinematics among the upper (until  
358 3  $\text{m.day}^{-1}$ ) and the lower (until 1  $\text{m.day}^{-1}$ ) parts becomes more evident than in the image plane.  
359 The geometrical effect induced by the presence of the stable *in-situ* crest on the landslide  
360 kinematics is also clearly pointed out. The temporal evolution of the displacement rates is  
361 illustrated with two transversal and one longitudinal profiles on Figures 9 and 10. The difference

362 of displacement rates between the upper and the lower part of the landslide is particularly pointed  
363 out.

364 The precision of the computed displacements is assessed by performing a null hypothesis on the  
365 stable areas (Berthier et al., 2005; Casson et al., 2003). Only the points with a correlation  
366 coefficient  $r > 0.8$  are taken into account. In the image plane coordinate system, the average errors  
367  $\mu$  range from 0.5 to 0.9 pixel with standard deviations  $\sigma$  of 0.3 to 1.2 pixel for the image pairs  
368 between the 20 May and the 25 June. In the local coordinate system, the average errors  $\mu$  range  
369 from 0.03 m to 0.11 m with standard deviations  $\sigma$  of 0.10 to 0.31 m for the image pairs between  
370 the 20 May and the 25 June.

## 371 **4.2 Comparison with DGPS displacements**

372 In order to estimate the accuracy and validate the calculated displacements, comparisons with  
373 independent and more accurate geodetic technique is necessary. Sixty benchmarks distributed in  
374 the stable parts and on the landslide body were monitored by DGPS with a horizontal and a  
375 vertical average accuracy of  $\pm 0.02$  m and  $\pm 0.05$  m. In total, 219 DGPS measurements are  
376 available for the period 2008–2009. In order to validate the displacements computed in the image  
377 plane, the DGPS benchmarks are projected in the image plane using the collinearity equations  
378 (Bonneval 1972, Kraus & Waldhäusel, 1998). The pixel displacements derived from the image  
379 correlation are then averaged in a perimeter of 16 pixels around each benchmark. The results are  
380 presented in Figure 11A. A correlation coefficient of  $r=0.98$  is found between DGPS  
381 measurements and Image Correlation, and an average relative accuracy of 11% is determined  
382 (Fig. 11C). In order to validate the metric displacements in the local coordinate system, the ortho-  
383 rectified displacements are averaged in an area of  $4 \text{ m}^2$  around each benchmark and compared  
384 with the DGPS displacements. A correlation coefficient of  $r=0.95$  is found (Fig. 11B), and an  
385 average relative accuracy of 20% is determined (Fig. 11D).

386

## 387 **5 Discussion: sources of errors**

388 The major sources of errors affecting the displacement calculations and thus potentially limiting  
389 the efficiency of the TOP for an operational landslide monitoring are the parameters affecting the  
390 Image Correlation computation and the external parameters influencing the ortho-rectification  
391 procedure.

## 392 **5.1 Sources of errors affecting the Image Correlation computation**

### 393 **5.1.1 Accuracy and precision of the Image Correlation algorithm**

394 One limitation of the Image Correlation technique is directly linked to the correlation algorithm  
395 used for matching the image pairs and to the sub-pixel interpolation method (Debella-Gilo &  
396 Kääb, 2010). The performance of a measurement system can be assessed by considering the  
397 errors associated in terms of accuracy and precision. In this section, the accuracy is represented  
398 by the average misfit between the measurements and the true value. Precision is represented by  
399 the standard deviation of the misfit between the measurements and the true value.

400 A series of experimental tests were carried out to assess the precision of the Image Correlation  
401 technique. The series of tests allow to investigate the influences of the size of the correlation  
402 window and of the level of noise observed in the images. Homogeneous imposed displacements  
403 (systematically equal to a multiple of pixels to avoid image resampling; Chambon & Schmittbuhl,  
404 2003) are applied to pairs of images to create synthetic images. Furthermore, three levels of  
405 Gaussian noise were added to the original images with a mean noise level imposed to zero and  
406 variances  $\sigma^2$  imposed to  $10^{-4}$ ,  $10^{-3}$  and  $10^{-2}$  (Fig. 12A). Then the Image Correlation technique is  
407 applied on the original image taken as reference and on the synthetic image with different sizes of  
408 correlation windows (5, 10, 16, 20, 30 and 50 pixels). For each correlation window, fifteen  
409 imposed displacements were realized with an amplitude ranging from 1 to 23 pixels along the  $u$   
410 and  $v$ -directions. The analysis was conducted by comparing the noisy synthetic images with the  
411 reference image. In the optimal case, the measured displacement would be identical to the  
412 imposed displacement.

413 Each Image Correlation analysis revealed displacement differences distributed close to zero  
414 (mean accuracy of  $5 \cdot 10^{-4}$  pixels). As observed by Hild et al. (2003), the precision of the  
415 correlation algorithm mainly depends on the pixel fraction of the displacement. Larger correlation  
416 windows produce less scattered displacements and therefore improve the precision. By plotting  
417 the standard deviation of the calculated displacements against the size of the correlation window,  
418 the influence of the correlation window size can be pointed out (Fig. 12B). For very low level of  
419 noise, the precision is less than 0.1 pixel for a size of correlation window greater than 5x5 pixels.  
420 For higher level of noise, the precision is more dependent on the size of the correlation window.  
421 Because homogenous displacements field were imposed in the image, the accuracy (average  
422 misfit) is similar for small and large correlation windows. In reality, the displacement field  
423 becomes more heterogeneous at higher resolution. Therefore, an increase of the size of the

424 correlation window implies a decrease of the displacement accuracy, but, as shown in these tests,  
425 an increase of the precision.

### 426 **5.1.2 Influence of ground surface state**

427

428 The time lag between two image acquisitions is one of the critical factors that affect the  
429 correlation computation. This time has to be long enough to increase the signal (e.g. landslide  
430 displacement) but short enough to preserve the tracked features (Berthier et al., 2005). Loading of  
431 the snowpack on the ground during Winter, surface erosion due to fast snow melting and the  
432 development of water-saturated ponds in Spring, weathering of the objects, growing of grass and  
433 large deformations are environmental processes that significantly modify the surface state during  
434 a year. Such correlation errors are characterized by very low correlation coefficients, very large  
435 displacement amplitudes or randomly-distributed displacement directions in comparison to the  
436 neighbor pixels (Fig. 13). On average, about 20 to 25% of the points are usable from one year to  
437 the next year (using a correlation window of 16\*16 pixels and with a correlation coefficient  
438 threshold of 0.8). Consequently, the construction of long time series of displacements with the  
439 image correlation technique is a difficult task for the site. The range of cumulated displacement  
440 rates observed over a period of 16 months (May 2008–September 2009) is illustrated by tracking  
441 the displacement at three locations in the upper (pt 1), middle (pt 2) and lower (pt 3) parts of the  
442 landslide at the direct vicinity of benchmark measured by DGPS (Figs. 9, 11). In our case, the  
443 cumulated displacements of the year 2009 are adjusted on those of 2008 using GCPs measured  
444 with DGPS at the vicinity of the points pt1, pt2 and pt3. The monitoring of a few benchmark with  
445 geodetic techniques is therefore necessary to combine displacement pattern observed in image  
446 pairs acquired over the period May 2008–September 2009 (74 pairs of images). After the  
447 acceleration period of Spring 2008, the displacement rates are decreasing to relative constant  
448 values of about 0.02 m.day<sup>-1</sup> in the lower and middle parts and 0.05 m.day<sup>-1</sup> in the upper part  
449 computed over the period July to October (Fig 14). Although these displacement rates are very  
450 close to the resolution of the image, the calculated displacements are in very good agreement with  
451 the displacement of the benchmarks measured by DGPS, demonstrating that the Image  
452 Correlation technique is an efficient technique to complement on-site measurements.

### 453 **5.1.3 Influence of illumination conditions**

454 The difference observed in RGB intensities in various images acquired with various solar  
455 illumination angles is an important limited factor essentially in terms of changes of the shadow

456 areas (Berthier et al., 2005). In order to assess the influence of illumination conditions on the  
457 image correlation results, two experiments are carried out.

458 The first experiment consists in correlating images acquired at different times within a day. Four  
459 photographs acquired 11:00, 12:00, 13:00 and 14:00 GMT in a period of small displacements  
460 (August 2009) and of clear sky conditions are correlated. The results indicate that illumination  
461 changes can lead to an average and a standard deviation of pixel-level error of respectively  
462  $\mu_{1h}=1.31$  and  $\sigma_{1h}=0.03$ ,  $\mu_{2h}=1.35$  and  $\sigma_{2h}=0.12$ ,  $\mu_{3h}=1.89$  and  $\sigma_{3h}=0.18$  pixel for time-interval  
463 acquisition of respectively 1, 2 and 3 hours. The results demonstrate that the correlation of images  
464 acquired in nearly similar illumination conditions can display a pixel-level precision.

465 The effect of illumination changes can be larger if the images are acquired at different seasons.  
466 This influence cannot be assessed by correlating images distant in time because of the landslide  
467 displacements. Therefore the second experiment consists in creating synthetic images with  
468 different shadow areas as a function of the sun azimuth and elevation (Burrough & McDonell,  
469 1988). Only the shadows created by direct solar illumination are analyzed assuming clear-sky  
470 conditions; the effects of reflected and diffuse illuminations are neglected. First, the shaded relief  
471 on the landslide is computed from the DEM in the local coordinate system. Then, the shaded  
472 relief is projected and linearly interpolated in the image plane coordinate system. 97 shaded relief  
473 images were created with different artificial illuminations. An example of shaded relief image is  
474 represented in Figure 5. Because a preference is given to correlate images taken when the sun  
475 elevation is maximal (Delacourt et al., 2007), a shaded relief image with a sun elevation of  $65^\circ$   
476 and a sun azimuth of  $250^\circ$  (illumination coming from the South-West) is chosen as the reference  
477 image for the correlation. It represents the illumination conditions on the landslide in the month  
478 of July at 12:00 GMT in clear sky conditions. The reference image is correlated with the shaded  
479 relief images, and the calculated displacements are compared to the errors induced by  
480 illumination changes. The mean displacement error and the mean correlation coefficient are used  
481 to characterize the influence of illumination changes on the image. Because only the shadow  
482 intensities are correlated, the errors are overestimated and are therefore represented by a  
483 normalized index.

484 As expected, the correlation of the synthetic images show that the correlation coefficient tends  
485 rapidly to  $r=1$  when the sun elevation is closer to the reference image (at 12.00 GMT) and the  
486 slope of the relationship depends on the sun azimuth (Fig. 15A). At the opposite, the correlation  
487 coefficient drops quickly when the illumination comes from the South-East (azimuth of  $120^\circ$ ) and  
488 shows a strong sensitivity to sun elevation changes. Low sun azimuth ( $120^\circ$ ) and low elevation  
489 angles ( $30^\circ$ ) typically represent illumination conditions at the end of the daytime which are thus

490 not optimal for the correlation. In addition, low sun elevations ( $30^\circ$ ) and higher azimuths ( $200^\circ$ )  
491 are typical illumination conditions of the autumn period at 12.00 GMT. These images are also not  
492 very relevant for the calculation of the displacements because the correlation coefficient is low.  
493 This finding is in agreement with Table 2 which indicates the amount of interpretable  
494 displacements is lower in the autumn season than in the summer season (lower correlation  
495 coefficients).

496 Figure 15B presents the mean correlation coefficient versus the displacement noise index. As  
497 expected, for sun azimuths equal to the reference image ( $240^\circ$ ), the displacement noise decreases  
498 with an increase of the correlation coefficient. In very bad illumination conditions (e.g. a low sun  
499 elevation and a sun azimuth opposite to the reference  $-100^\circ$ ), the trend is inversed because the  
500 image becomes very low textured (most areas of the landslide are in the shadow with  
501 homogeneous intensity values). In that case, no maximum correlation value is computed,  
502 resulting in a null displacement with the correlation algorithm used in this study. Similar results  
503 are observed for images displaying homogeneous texture such as for instance in backlighting  
504 conditions, in foggy meteorological conditions or when the ground surface is covered by snow.  
505 Therefore, correlation of images with a too important time-lapse has to be avoided to minimize  
506 illumination effects. A possible alternative is to correlate images under diffused illumination  
507 (cloudy day) thus providing a more homogenous lighting. At the opposite, correlation of images  
508 acquired at the same solar time in the day and when the sun elevation is maximal is optimal.

## 509 **5.2 Sources of errors affecting the ortho-rectification procedure**

### 510 **5.2.1 Influence of camera orientation**

511 The accuracy camera orientation is a parameter affecting both the image geometry and the  
512 accuracy of the geo-referencing (Mikhail et al., 2001). If changes in external orientations of the  
513 camera are small, the image geometry is not significantly affected. Consequently a homogeneous  
514 component in the correlated displacement field is visible in the image plane (Fig. 16A). This  
515 misfit can be significant in the areas where the expected displacements are low or null such as in  
516 the stable parts. This systematic error can be corrected assuming a rigid translation of the image  
517 by removing the average  $\Delta u$  and  $\Delta v$  misfits (observed on the stable parts of the images such as  
518 stable crests or on reference targets located outside the landslide; Fig. 2B, A; Fallourt et al.,  
519 2010). Nevertheless this correction is not fully optimal, because the geometric deformations  
520 caused by the slight orientation changes of the camera depend on the object distance. Therefore,

521 after correction of the homogeneous component in the image plane, an average residual misfit of  
522 about 0 to 2 pixels is observed .

523 In order to evaluate the accuracy of the external orientation that influences the georeferencing  
524 quality, fourty GCPs not introduced in the minimization processes of section §3.2.3 are used. The  
525 shift between the projected and the observed GCPs positions in the image plane is thus  
526 determined (Fig. 16B). A mean shift error of, respectively, -0.20 and -0.08 pixel with a standard  
527 deviation of 1.59 and 1.51 pixels in the  $u$  and  $v$ -directions respectively is obtained (Table 4). The  
528 accuracy of the external parameters in the georeferencing procedure in the local coordinate  
529 system is calculated by comparing the back-projected GCPs identified in the image plane with the  
530 GCPs positions measured with DGPS and located in the stable parts. The absolute accuracy in  $X$ ,  
531  $Y$  and  $Z$  coordinates are presented in Table 4. Because most of GCPs in the stable parts are  
532 located in the background of the image (750 m from the camera location) where the ground pixel  
533 size is about 20 cm, the mean 3D error (0.14 m) and the standard deviation (0.56 m) of the  
534 positioning are not representative of the areas of the landslide located closer to the camera  
535 (300 m). Nevertheless, because the standard deviation of the GCP located in the image plane are  
536 close to the accuracy of the GCPs picking, the determination of the camera orientation is  
537 considered acceptable. Furthermore, the good coherence between the shaded relief images  
538 (Fig. 5) and the true images (Fig. 2A) shows that the quality of the determination of the camera  
539 orientation is satisfying.

### 540 **5.2.2 Influence of the DEM**

541 The accuracy of the DEM used in the ortho-rectification procedure is important to correct large  
542 distortion induced by the topography, which in turn controls the accuracy of the displacements in  
543 the local coordinate system. Therefore, the actual necessity of using a mono-temporal DEM for  
544 the complete series of image pairs has to be addressed. In order to evaluate its influence on the  
545 ortho-rectified displacements, the displacements of the 1<sup>st</sup> June–4<sup>th</sup> June 2008 originally ortho-  
546 rectified with the DEM of October 2007 (Fig. 9) are compared with those orthorectified with the  
547 DEM of July 2009 documenting a slightly different landslide morphology (Fig. 17A, B). The  
548 observed differences in displacement are presented relative to the displacement orthorectified  
549 with the DEM of 2007. The differences vary spatially in the landslide area. Despite some areas  
550 displaying differences in displacement larger than 75%, the average difference is 21% which is  
551 very similar to the differences observed with the DGPS measurements (Fig. 11D). As a  
552 consequence, the influence of the DEM on the accuracy of the displacement is more important  
553 than the influence of the camera orientation, the image resolution and changes in illumination

554 conditions. For large displacements, morphologic changes become significant and the errors on  
555 the displacements increase. The computation of multi-temporal DEMs for each image is therefore  
556 a pre-requisite to improve the accuracy of the ortho-rectified displacements. Nevertheless, in case  
557 of a translational landslide characterized by low changes in elevation, the use of the same DEM  
558 constitutes still an acceptable 1<sup>st</sup>-order estimate.  
559

## 560 **6 Conclusion**

561 The potential of multi-temporal correlation of ground-based images for landslide monitoring has  
562 been assessed using the dataset available on the Super Sauze landslide (South French Alps). A  
563 methodology to compute displacement rates both in the image plane coordinate system and in the  
564 local coordinate system has been proposed.

565 The results demonstrated clearly the potential and the limitation of this technique by identifying  
566 the heterogeneous displacement field, in space and in time, of the landslide. The camera  
567 monitoring allowed to characterize displacements up to 3 m.day<sup>-1</sup> during an acceleration period,  
568 and displacement of about 0.02 m.day<sup>-1</sup> computed over the period July to September (the less  
569 active period). The results are in good agreement with previous knowledge on the landslide  
570 kinematics and are in very good agreement with benchmark displacements measured by DGPS.

571 For objects located in a range of 300 to 900 m from the camera location, this study showed that  
572 the pixel size can vary from 0.005 to 0.04 m<sup>2</sup> according to the resolution of the image (2000x3008  
573 pixels) and the angle of incidence of the line of sight. The orientation of the line of sight  
574 (depending on the location and orientation of the camera) to the ground surface has to be  
575 considered before installing a permanent monitoring system. Areas of low incidence angles (< 5°)  
576 are very sensitive to small movements of the camera. Therefore, the angle should be the most  
577 perpendicular as possible to the mean displacement vector of the landslide. 3D displacements of  
578 less than 0.04 m and 0.06 m in the lower part of the landslide and 0.09 m and 0.11 m in the *u* and  
579 *v*-directions are difficult to measure over a period of four days without a sub-pixel correlation  
580 algorithm.

581 The strongest limitations are independent of the acquisition system and are related to the  
582 meteorological and illumination conditions and the ground surface changes inducing partial or  
583 complete loss of coherence between pairs of images. During the winter season (from November  
584 to May), the presence of snow impedes reliable correlation results and excessive ground  
585 deformations between two consecutive years impede valid displacement measurements even if  
586 the images are acquired during the same solar time. The small changes in the camera orientation

587 and the use of a constant DEM are the most important parameters that affect the accuracy of the  
588 ortho-rectification of the displacement field. A regular acquisition of multi-temporal DEMs  
589 through airborne or terrestrial laser scanning or stereoscopic photogrammetric views is believed  
590 to be a priority to significantly improve the accuracy of the technique. The errors induced by the  
591 sub-pixel correlation algorithm are thus insignificant compared to the influences of the other  
592 parameters cited previously.

593 The results demonstrate that Image Correlation techniques implemented in permanent monitoring  
594 system is particularly interesting for monitoring landslides characterized by annual pluri-  
595 decimetric displacements. In addition, this low cost technique is a very suitable alternative for  
596 inaccessible landslides or areas without access to power supply. Furthermore, because the  
597 proposed methodology does not require GCPs except for determining the external orientation of  
598 the camera and for combining displacement pattern observed in image pairs acquired over two  
599 years, the methodology can be routinely and automatically applied to new pairs of images.  
600 Therefore this study offers very promising perspectives for operational applications which can be  
601 potentially integrated in an early warning system by considering additional efforts in direct data  
602 transmission. Finally, inversion of the displacement field could be developed to characterize the  
603 macroscopic rheological properties of the landslide material.

604

## 605 **Acknowledgements**

606 This work was supported by the European Commission within the Marie Curie Research and  
607 Training Network '*Mountain Risks: from prediction to management and governance*' (2007-  
608 2010, Contract MCRTN-035798) and by the FP7 Large-scale Integrating Project '*Safeland:  
609 Living with landslide risk in Europe*' (2009-2012, Contract 226479). The ortho-images and the  
610 airborne LiDAR data of the Super-Sauze landslide have been acquired by the Helimap System  
611 service in 2009. The authors would like to acknowledge André Stumpf (University of Strasbourg,  
612 France & University of Twente, Netherlands) and Sabrina Rothmund (University of Stuttgart,  
613 Germany) for their help in the field. Special thanks are also due to Bas van Dam (Utrecht  
614 University, Netherlands) who designed the automatic monitoring system.

615

616

## 617 **References**

618 Alaoui El. M. I., & Ibn-Elhaj E. (2009). A robust hierarchical motion estimation algorithm in  
619 noisy image sequences in the bispectrum domain. *Signal Image and Video Processing*, 3,  
620 291-302.

621 Anandan, P., Bergen, R.J., Hanna, K.J., & Hanna, K.J. (1993). Hierarchical model-based motion  
622 estimation. In L. Sezan, (Eds.), *Image Sequence Analysis*. Kluwer, Dordrecht.

623 Antonello, G., Casagli, N., Farina, P., Leva, D., Nico, G., Sieber, A.J., & Tarchi, D. (2004).  
624 Ground-based SAR interferometry for monitoring mass movements. *Landslides*, 1, 21-28.

625 Baratoux, D., Delacourt, C., & Allemand, P. (2001). High-resolution digital elevation models  
626 derived from Viking Orbiter images: Method and comparison with Mars Orbiter Laser  
627 Altimeter Data. *Journal of Geophysical Research*, 106, 32927-32941.

628 Bastard M., (2009). Caractérisation de la cinématique de glissement de terrain par technique de  
629 corrélation d'image optique. Master thesis. University of Strasbourg (EOST). Institut de  
630 Physique du Globe, Strasbourg, France.

631 Berthier, E, Vadon, H., Baratoux, D., Arnaud, Y., Vincent, C., Feigl, K. L., Rémy, F., & Legrésy  
632 B. (2005). Surface motion of mountain glaciers derived from satellite optical imagery.  
633 *Remote Sensing of Environment*, 95, 14-28.

634 Besl, P., & McKay, N. (1992). A method for registration of 3-D shapes. *IEEE Transactions on*  
635 *Pattern And Machine Intelligence*, 14, 239-256.

636 Bitelli G., Dubbini M., & Zanutta A. (2004). Terrestrial laser scanning and digital  
637 photogrammetry techniques to monitor landslides bodies, *International Archives of*  
638 *Photogrammetry, Remote Sensing and Spatial Information Sciences* 35, 246–251.

639 Bonneval, H., (1972). Levés topographiques par photogrammétrie aérienne. In Eyrolles (Eds.),  
640 *Photogrammétrie générale: Tome 3, Collection scientifique de l'Institut Géographique*  
641 *National*, Paris, France.

642 Brunner, F., Macheiner, K., & Woschitz, H. (2007). Monitoring of deep-seated mass movements.  
643 *Proceedings of the 3rd International Conference on Structural Health Monitoring of*  
644 *Intelligent Infra-structure*, Vancouver, Canada.

645 Burrough, P. A., & McDonell, R.A. (1998). *Principles of Geographical Information Systems*  
646 ,Oxford University Press, New York.

647 Casagli, N., Farina, P., Leva, D., & Tarchi, D. (2004). Application of ground-based radar  
648 interferome-try to monitor an active rock slide and implications on the emergency  
649 management. In E. Kluwer (Eds.), *The NATO Advanced Research Workshop*, Celano, Italy.

650 Casson, B., Baratoux, D., Delacourt, D., & Allemand, P. (2003). “La Clapière” landslide motion  
651 observed from aerial differential high resolution DEM. *Engineering. Geology*, 68, 123-139.

652 Casson B., Delacourt C., & Allemand, P. (2005). Contribution of multi-temporal sensing images  
653 to characterize landslide slip surface – Application to the La Clapière Landslide (France).  
654 *Natural Hazards and Earth System Sciences*, 5, 425-437.

655 Cardenal, J., Mata, E., Perez-Garcia, J.L., Delgado, J., Andez, M.A., Gonzalez, A., Diaz-de-  
656 Teran, J.R. (2008). Close Range Digital Photogrammetry Techniques applied to Landslide  
657 Monitoring. International Archives of the Photogrammetry, *Remote sensing and Spatial*  
658 *Information Sciences*. Vol XXXVII. Part B8.

659 Chambon G. (2003). Caractérisation expérimentale du frottement effectif des zones de faille. PhD  
660 Thesis. Université Paris XI Orsay, ENPC..

661 Chambon, G., & Schmittbuhl, J. (2003). Shear with comminution of a granular material:  
662 Microscopic deformations outside the shear band. *Physical Review E*, 68, 1-8.

663 Corripio, J.G. (2004). Snow surface albedo estimations using terrestrial photography.  
664 *International Journal of Remote Sensing*, 25(24), 5705-5729.

665 Corsini, A., Farina P., Antonello G., Barbieri M., Casagli N., Coren F., Guerri L., Ronchetti F.,  
666 Sterzai P., & Tarchi D. (2006). Space-borne and ground-based SAR interferometry as tools  
667 for landslide hazard management in civil protection. *International Journal of Remote*  
668 *Sensing*, 27, 2351 - 2369.

669 D’Antone, I. (1995). Hierarchical correlation for track finding. *Nuclear Instrument and Methods*  
670 *in Physics Research*, 356, 476-484.

671 Debella-Gilo M., & Kääb A. Sub-pixel precision image matching for measuring surface  
672 displacements on mass movements using normalized cross-correlation. *Remote Sensing of*  
673 *Environment* (2010).

674 Delacourt, C., Allemand P., Casson B., & Vadon H. (2004). Velocity field of the “La Clapiere”  
675 landslide measured by the correlation of aerial and Quick-Bird satellite images. *Geophysical.*  
676 *Research Letters*, 31, 1-5.

677 Delacourt, C., Allemand, P., Berthier, E., Raucoules, D., Casson, B., Grandjean, P., Pambrun, C.,  
678 & Varel, E. 2007. Remote-sensing techniques for analysing landslide kinematics: a review.  
679 *Bulletin de Société Géologique*, 178, 89-100.

680 Fallourd, R., Vernier, F., Friedt J.-M., Martin, G., trouvé, E., Moreau, L. & Nicolas, J.-M. (2010).  
681 Monitoring temperate glacier with high resolution automated digital cameras – Application to  
682 the Argentière Glacier. in: Paparoditis N., Pierrot-Deseilligny M., Mallet C. & Tournaire O.  
683 (Eds.), IAPRS, Vol. XXXVIII, Part 3B, Saint-Mandé, France., 1-23.

684 Fisher, P.F. (1991). First experiments in viewshed uncertainty: The accuracy of the viewshed  
685 area. *Photogrammetric Engineering Remote Sensing*, 57, 1321-1327.

686 Foppe, K., Barth, W., & Preis, S. (2006). Autonomous Permanent Automatic Monitoring System  
687 with Robot-Tacheometers. *Proceedings of the XXIII International FIG Congress*, Munich,  
688 Germany.

689 Franklin, W.R., & C.K. Rav. (1994). Higher isn't necessarily better: Visibility algorithms and  
690 experiments, *Proceedings of the 6<sup>th</sup> International Symposium on Spatial Data Handling*,  
691 Edinburgh, Scotland, 2, 751-770.

692 Heikkila, J., & Silven, O. (1997). A four-step camera calibration procedure with implicit image  
693 correction. *IEEE Computer. Society*, 1106-1112.

694 Hemmleb, M., & Wiedemann, A. (1997). Digital Rectification and Generation of Orthoimages in  
695 Architectural Photogrammetry. *CIPA International Symposium*, IAPRS, XXXII, Part 5C1B  
696 (pp. 261-267), Göteborg, Sweden.

697 Hild F. (2003). Mesure de champs de déplacement par corrélation d'images et applications en  
698 mécanique des solides. *Notes de cours IPSI*. Laboratoire de Mécanique et Technologie,  
699 CNRS-UMR 8535, Université Paris 6, France.

700 Honda, K., & M. Nagai (2002), Real-time volcano activity mapping using ground-based digital  
701 imagery, *ISPRS Journal of Photogrammetry and Remote Sensing*, 57,1-2, 159-168.

702 Jaboyedoff M., Ornstein P., & Rouiller J.-D. (2004). Design of a geodetic database and associated  
703 tools for monitoring rock-slope movements: the example of the top of Randa rockfall scar.  
704 *Natural Hazards and Earth System Science*, 4, 187-196.

705 Jaboyedoff, M., Oppikofer T., Abellan A., Derron M.-H., Loye A., Metzger R., & Pedrazzini A.  
706 (2010). Use of LiDAR in landslide investigations: a review. *Natural Hazards*. doi  
707 10.1007/s11069-010-9634-2

708 Jiang, R., Jauregui, D.V., & White, K. (2008). Close-range photogrammetry applications in  
709 bridge measurement: Literature review. *Measurement*, 41, 823-834.

710 Kraus, K. & Waldhäusl, P., (1994). *Photogrammetry, Fundamentals and Standard processes*. vol  
711 1. Hermès (editor), Paris.

712 Kumar, S., & Banerjee, S., (1998). Development and application of a hierarchical system for  
713 digital particle image velocimetry to free-surface turbulence. *Physics of Fluids*, 10, 160-177.

714 Küntz, M., Jolin, M., Bastien, J., Perez F., & Hild, F. (2007). Digital image correlation analysis of  
715 cracks behavior in a reinforced concrete beam during a load test. *Canadian journal of civil  
716 engineering*, 33, 1418-1425.

717 LePrince, S., Berthier, E., Ayoub, F., Delacourt, C., & Avouac, J.- P. (2008). Monitoring Earth  
718 Surface Dynamics With Optical Imagery. *Eos*, 89, 1-5.

719 Lewis, J.P., (1995). Fast normalized cross-correlation. *Vision Interface*, 120-123.

720 Lim, M., Petley, D.N., Rosser, N.J., Allison, R.J., Long, A.J. & Pybus, D. (2005). Combined  
721 digital photogrammetry and time-of-flight laser scanning for monitoring cliff evolution. *The*  
722 *Photogrammetric Record*, 20, 109-129.

723 Luzi, G., (2010). Ground based SAR interferometry: a novel tool for Geoscience. In:  
724 Geoscience and Remote Sensing, New Achievements, P.Imperatore & D. Riccio (Editors),  
725 ISBN: 978-953-7619-97-8. In print.

726 Malet, J.-P., Maquaire, O., & Calais, E. (2002). The use of global positioning system techniques  
727 for the continuous monitoring of landslides. *Geomorphology*, 43, 33-54.

728 Malet, J.-P. (2003). Les glissements de type écoulement dans les marnes noires des Alpes du Sud.  
729 Morphologie, fonctionnement et modélisation hydromécanique. PhD Thesis in Earth  
730 Sciences, Université Louis Pasteur, Strasbourg.

731 Mantovani, F. Soeters R., & van Western C.J. (1996). Remote sensing techniques for landslide  
732 studies and hazard zonation in Europe. *Geomorphology*, 15, 213-225.

733 Maas, H.-G., Schwalbe, E., Dietrich, R., Bäessler, M., & Ewert, H. (2008). Determination of  
734 spatio-temporal velocity fields on glaciers in West- Greenland by terrestrial image sequence  
735 analysis. *IAPRS*, XXXVII, Part B8 Beijing,China, 1419-1424.

736 Meissl, A., & Naterop, D. (1995). Automatic Measuring System for Permanent Monitoring –  
737 Solexperts GeoMonitor. *Proceedings of Field Measurements in Geomechanics 4th*  
738 *International Symposium*, Bergamo, Italy, 489-494.

739 Mikhail, E., Bethel, J. S., & McGlone, J. C. (2001). *Introduction to Modern Photogrammetry*,  
740 Hardcover (edition), New-York.

741 Monserrat, O., & Crosetto, M. (2008). Deformation measurement using terrestrial laser scanning  
742 data and least squares 3D surface matching. *ISPRS Journal of Photogrammetry and Remote*  
743 *Sensing*, 63, 142-154.

744 Moore J.F.A. (1992). Monitoring Building Structures. Blackie & Son Ltd. 155 p. ISBN 0-216-  
745 93141-X.

746 Oppikofer T., Jaboyedoff M., & Kreuzen H-R. (2008). Collapse at the eastern Eiger flank in the  
747 Swiss Alps. *Nature Geoscience*, 8, 531-535.

748 Pesci A., Baldi B., Bedin A., Casula G., Cenni N., Fabris M., Loddo F., Mora P., & Bacchetti M.  
749 (2004). Digital elevation models for landslide evolution monitoring: application on two areas  
750 located in the Reno River Valley (Italy). *Annals of Geophysics*, 47, 1339-1353.

751 Prokop, A., & Panholzer, H. (2009). Assessing the capability of terrestrial laser scanning for  
752 monitoring slow moving landslides. *Natural Hazards and Earth System Sciences*, 9, 1921-  
753 1928.

- 754 Rohaly J., Frigerio F., & Hart D. P. (2002). Reverse hierarchical PIV processing. *Measurement*  
755 *Science and Technology*, 13, 984-996.
- 756 Squarzoni C., Delacourt C., & Allemand P. (2005). Differential single-frequency GPS monitoring  
757 of the La Valette landslide (French Alps). *Engineering Geology*, 79, 215-229.
- 758 Sturzenegger, M., & Stead, D. (2009). Close-range terrestrial digital photogrammetry and  
759 terrestrial laser scanning for discontinuity characterization on rock cuts. *Engineering*  
760 *Geology*, 106, 163-182.
- 761 Tarchi, D., Casagli, N., Fanti, R., Leva, DD., Luzi, G., Pasuto, A., Pieraccini, M., & Silvano, S.  
762 (2003). Landslide monitoring by using ground-based SAR interferometry: an example of  
763 application to the Tessina landslide in Italy. *Engineering Geology*, 68, 15-30.
- 764 Teza, G., Galgaro, A., Zaltron, N., & Genevois, R. (2007). Terrestrial laser scanner to detect  
765 landslide displacement fields: a new approach, *International Journal of Remote Sensing*, 28,  
766 3425-3446.
- 767 Teza, G., Pesci, A., Genevois, R., & Galgaro, A. (2008). Characterization of landslide ground  
768 surface kinematics from terrestrial laser scanning and strain field computation.  
769 *Geomorphology*, 97, 424– 437.
- 770 Travelletti, J & Malet, J-P. Characterization of the 3D geometry of flow-like landslides: a  
771 methodology based on the integration of multi-source data. *Submitted in Engineering*  
772 *Geology*.
- 773 Wangensteen, B., Guomundsson, A., Eiken, T., Kääh, A., Farbrot, H., & Etzelmüller, B. (2006).  
774 Surface displacements and surface estimates for creeping slope landforms in Northern and  
775 Eastern Iceland using digital photogrammetry. *Geomorphology*, 80, 59-79.
- 776 White, D. J., Take, W. A. & Bolton, M. D., (2003). Soil deformation measurement using particle  
777 image velocimetry (PIV) and photogrammetry. *Géotechnique*, 53, 619-631.

## Figures

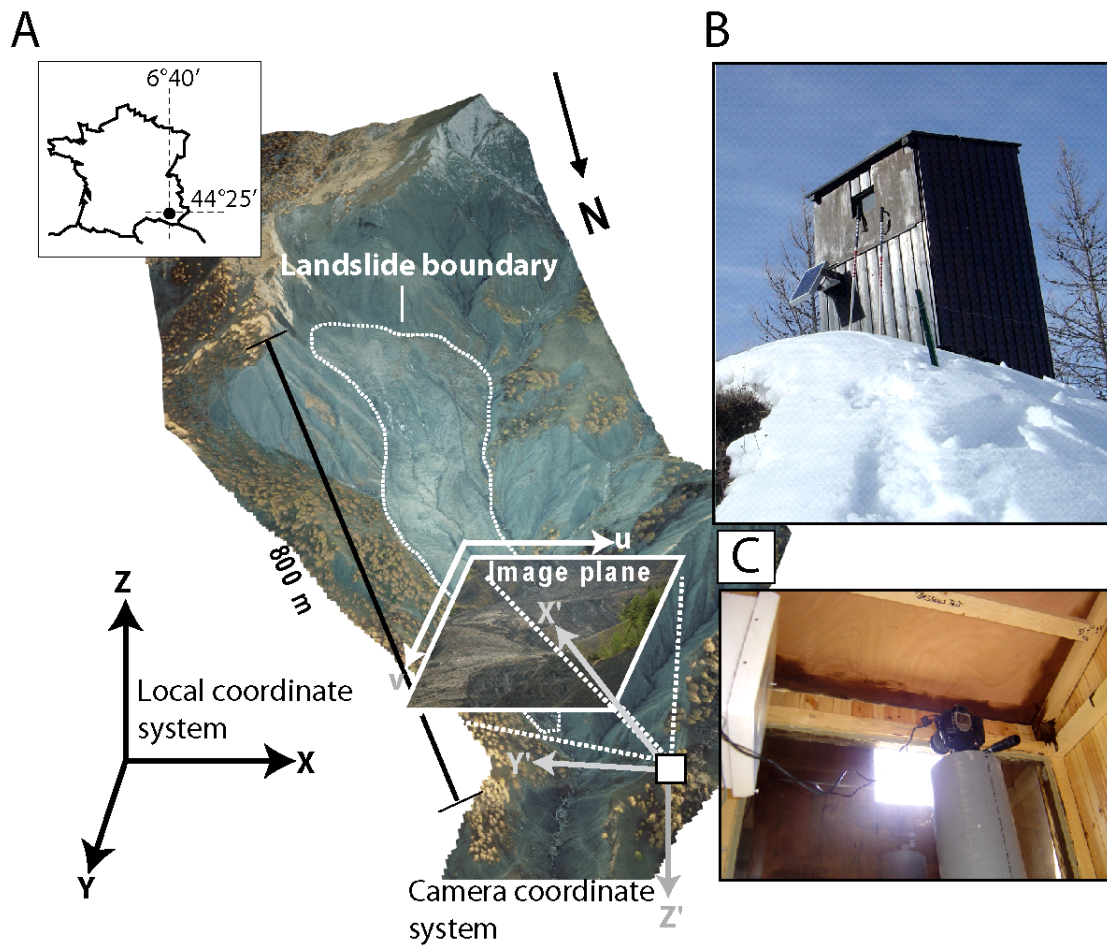


Fig. 1. (A) View of the Super-Sauze landslide towards the south with the different coordinate systems used in the georeferencing procedure. (B) Location of the camera monitoring system (C)

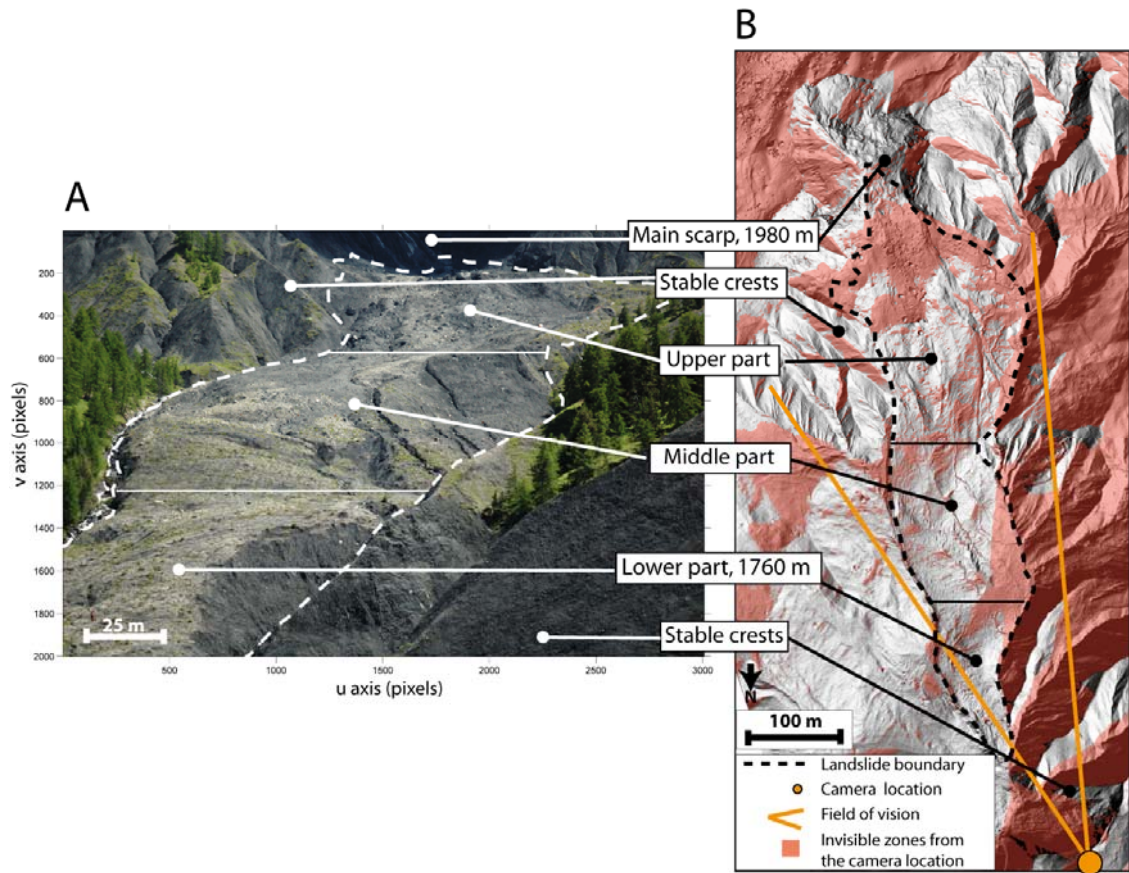


Fig. 2. Views of the landslide in the image geometry and in the local coordinate system (A) Image acquired by the monitoring system showing the different parts of the landslide from the camera location. (B) View of the landslide morphology in the local coordinate system on a shaded relief computed with a 0.25 m mesh DEM interpolated from airborne-LiDAR data sets acquired in July 2009. The invisible areas from the camera location are also shown.

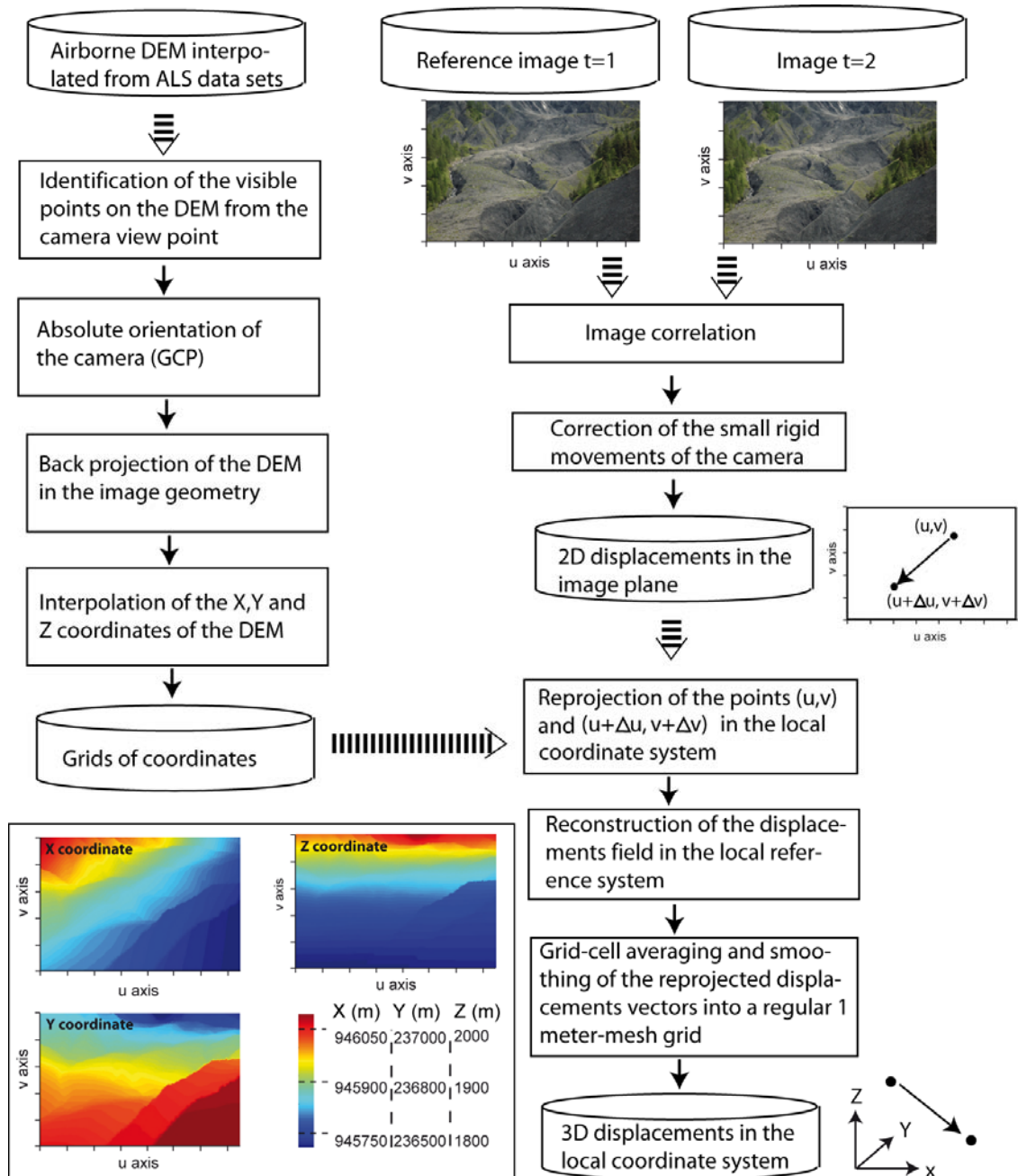


Fig 3. Flowchart of the methodology

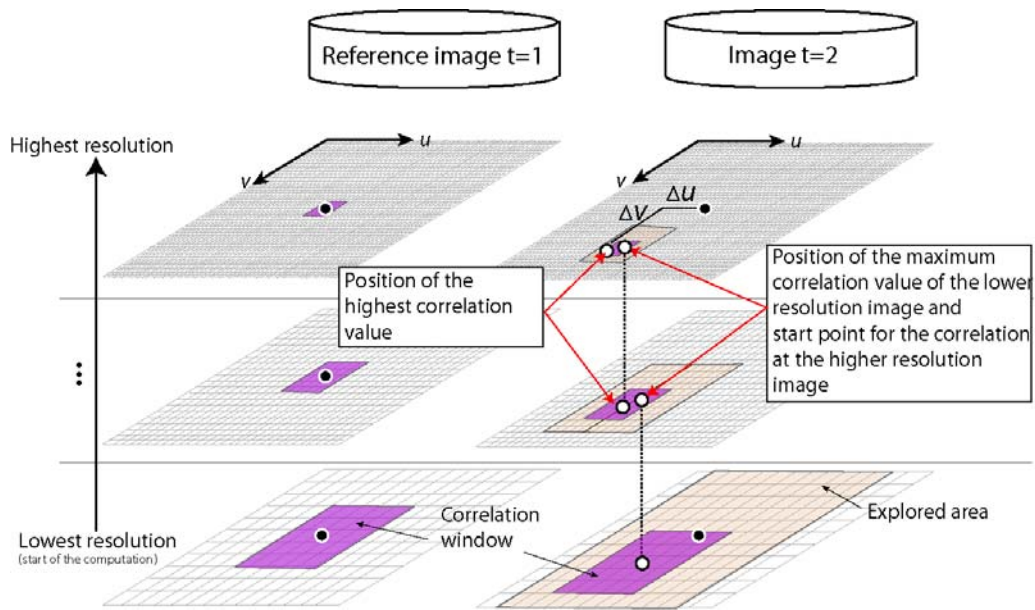


Fig. 4. Principle of the normalized hierarchical image correlation. The correlation computation starts from the lowest resolution to the highest resolution by keeping constant the size of the correlation window and the explored area, while their physical size is decreasing. At each higher resolution level, the explored area is centered on the pixel with the highest  $t$  correlation value of the previous resolution level. The estimate of the position of the maximum correlation value is thus increased.

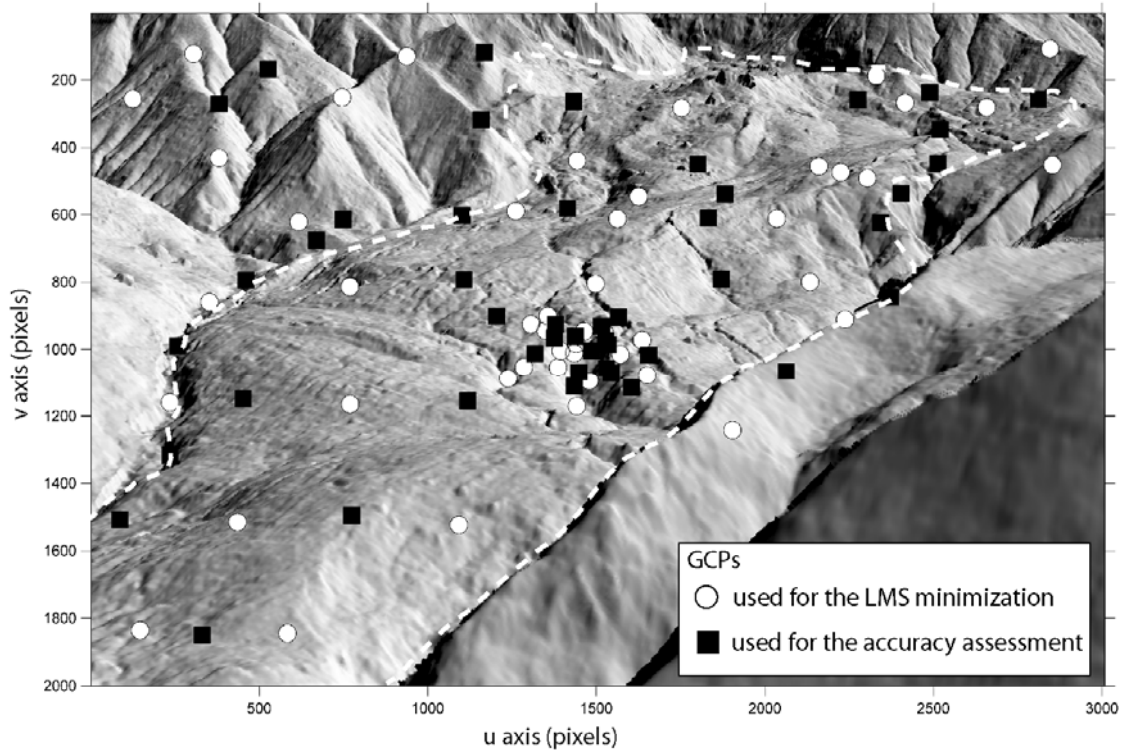


Fig.5. Location of the GCPs used for the Least Mean Square minimization (LMS) and for the accuracy analysis in a shaded relief image. The shaded relief image is produced by interpolating the shaded relief values of the DEM of 2009 projected in the image plane. This image is useful to visually check the quality of the back projection by comparison with a real image.

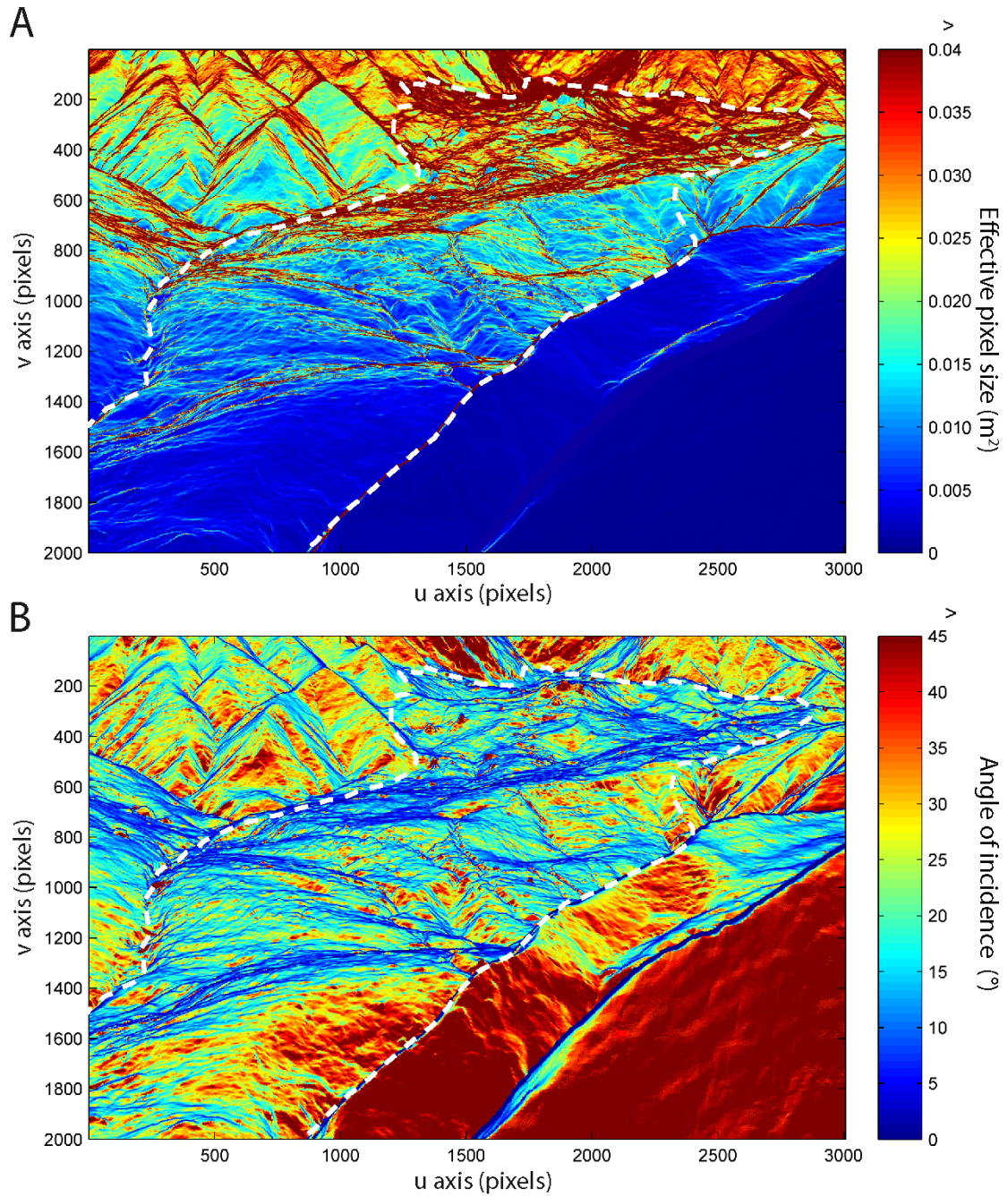


Fig. 6. Image resolution characteristics: (A) Effective pixel size in square meters (B) Angle of incidence in degrees. A low angle means that the line of sight is nearly tangential to the topography.

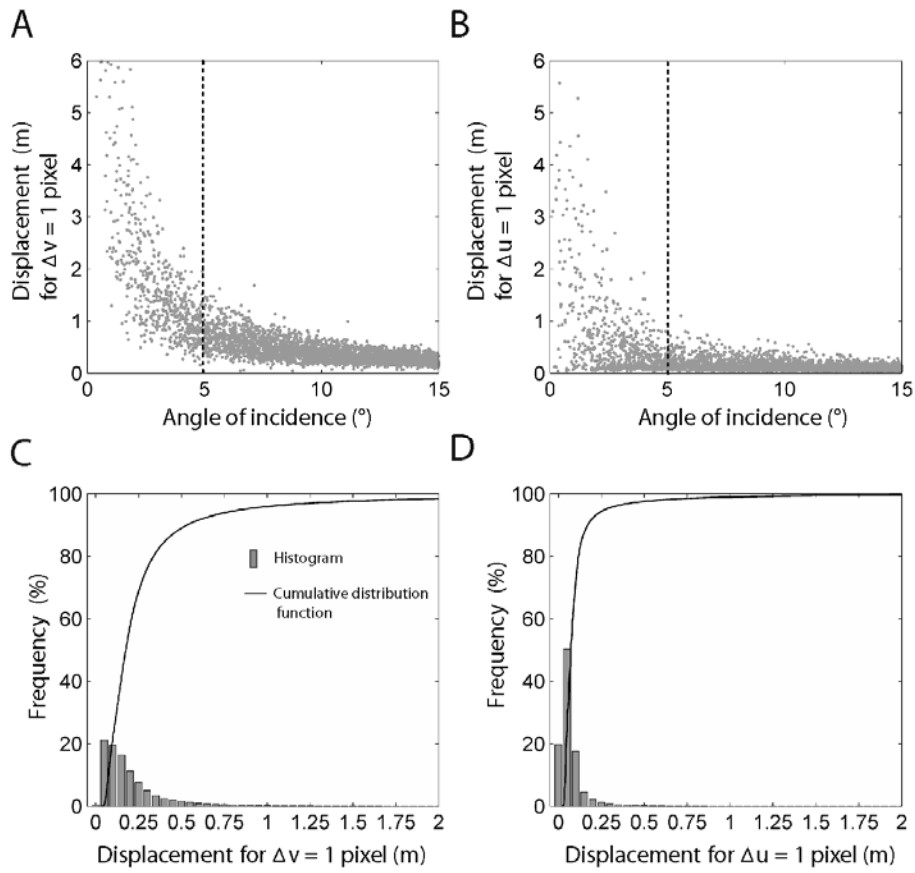


Fig. 7. Minimum metric displacement for pixel accuracy in v-axis (A) and u-axis (B) according to the angle of incidence. The sensitivity of metric displacements to small changes in u and v directions drastically increases for angle of incidence below  $5^\circ$ . (C) and (D) histograms and cumulative distribution function of the metric displacements resulting for 1 pixel displacement in v-axis and u-axis. 50% of the pixels in the image plane inside the landslide area shows a metric sensitivity less than 0.17 m for 1 pixel displacement in v-axis and 0.07 m in u-axis.

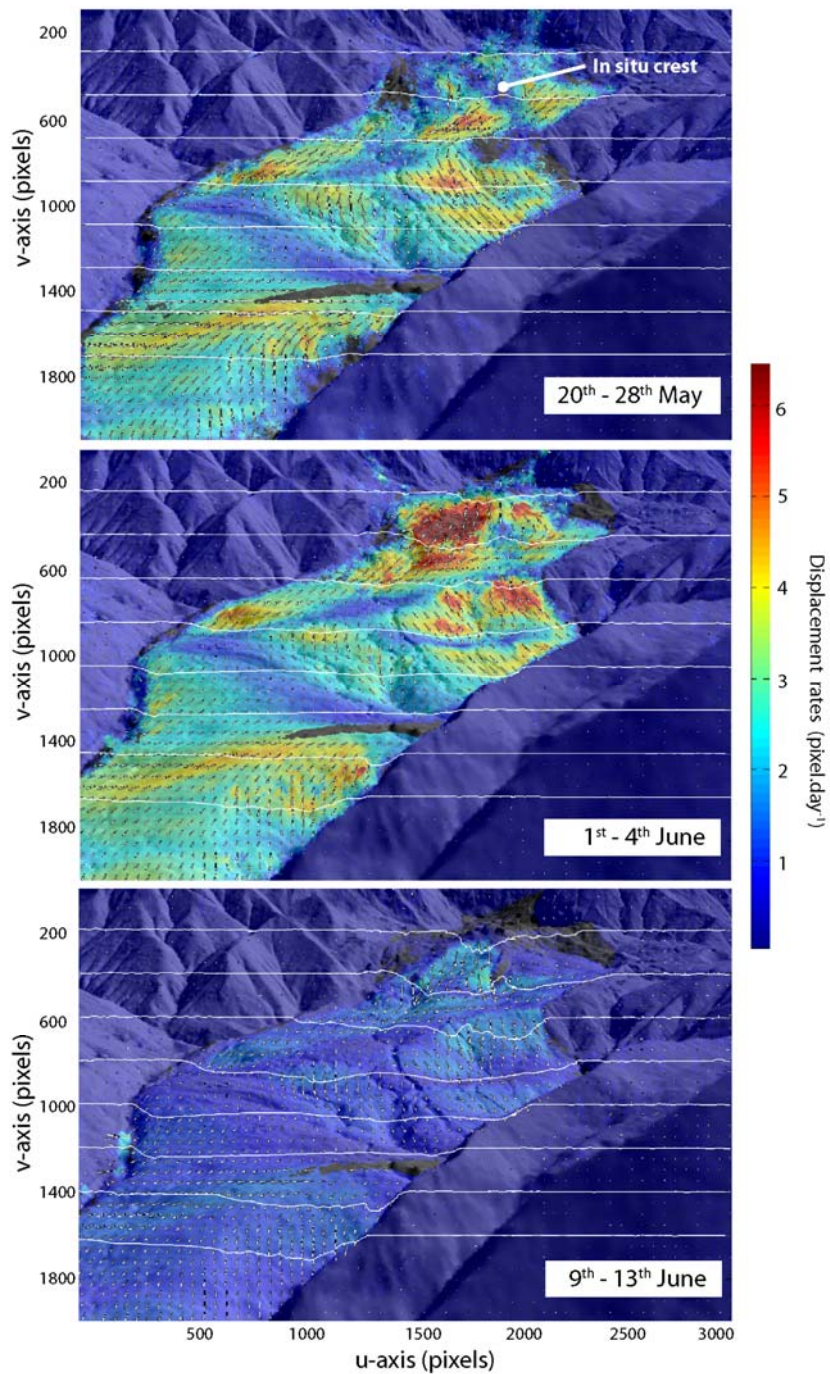


Fig. 8. Displacement rates amplitude (color) and displacement direction (arrows) in the image plane and cumulated displacements along 8 profiles crossing the landslide over the period the 20<sup>th</sup> May to the 25<sup>th</sup> June 2008. In order to highlight the displacement direction, the arrow length is normalized in each image.

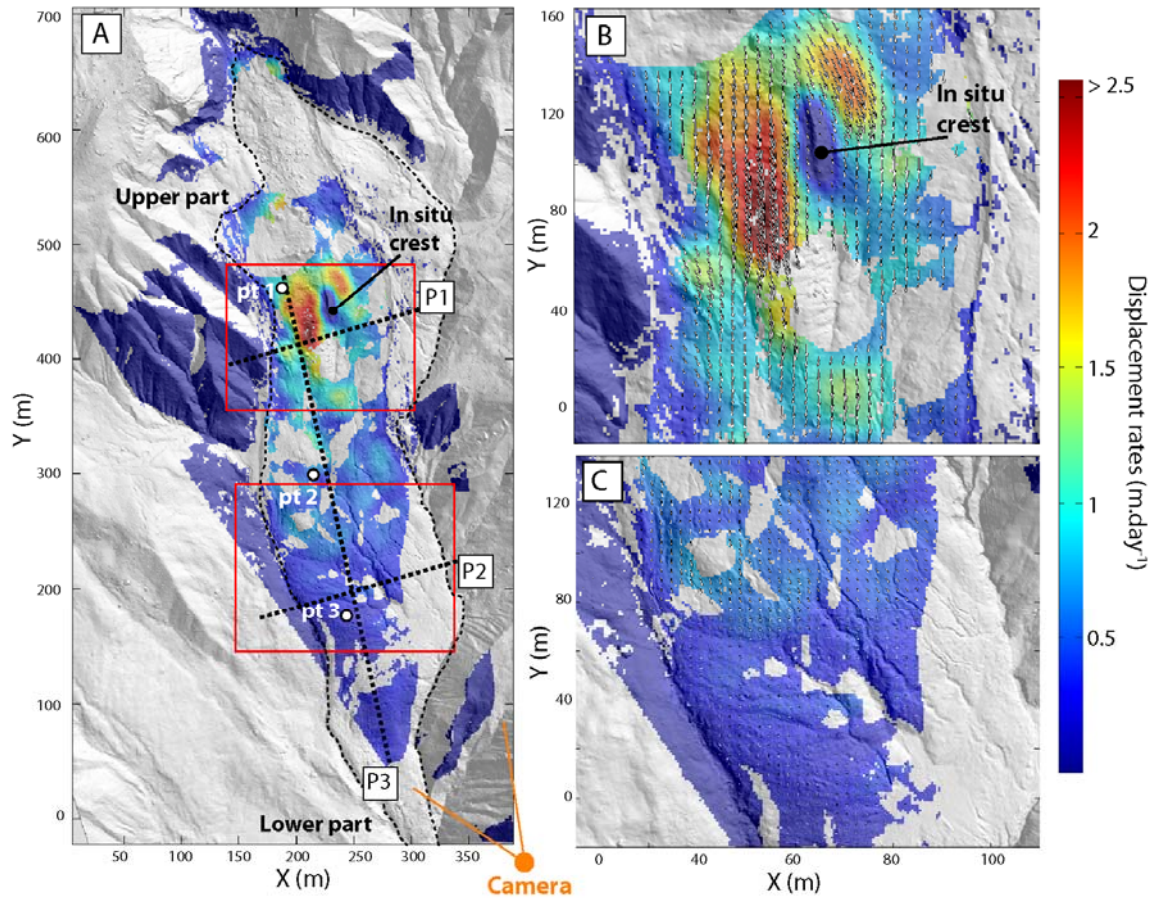


Fig. 9. Displacement rates map for the period 1<sup>st</sup> – 4<sup>th</sup> June 2008. (A) Displacement rates observed on the whole landslide. The profiles P1, P2 and P3 refer to Fig. 10 and the locations pt 1, pt 2 and pt 3 refer to Fig. 11. (B) Details on the displacement rates and displacement direction of the velocity amplitude and direction in the upper part. (C) Details on the displacement rates and displacement direction in the lower part.

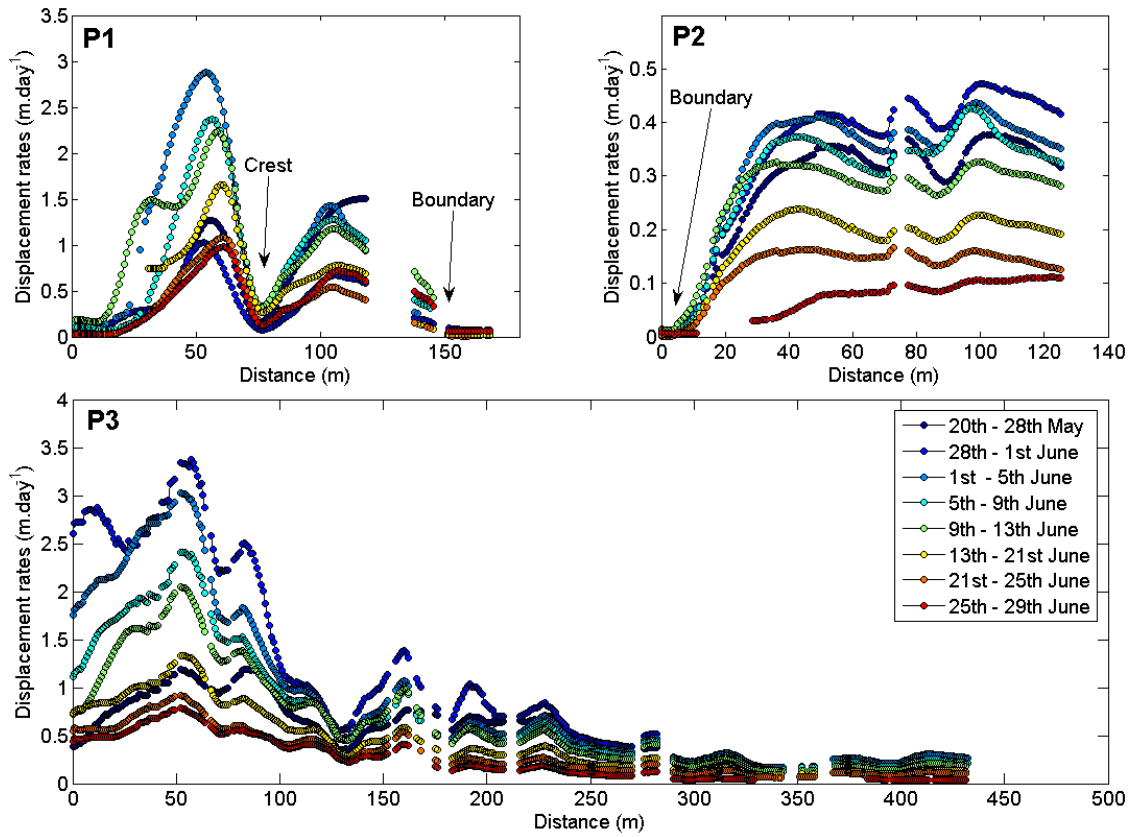


Fig. 10. Displacement rates profiles in the upper (P1), the medium (P2) and the lower (P3) part of the landslide. The location of the profiles is indicated in Fig. 9.

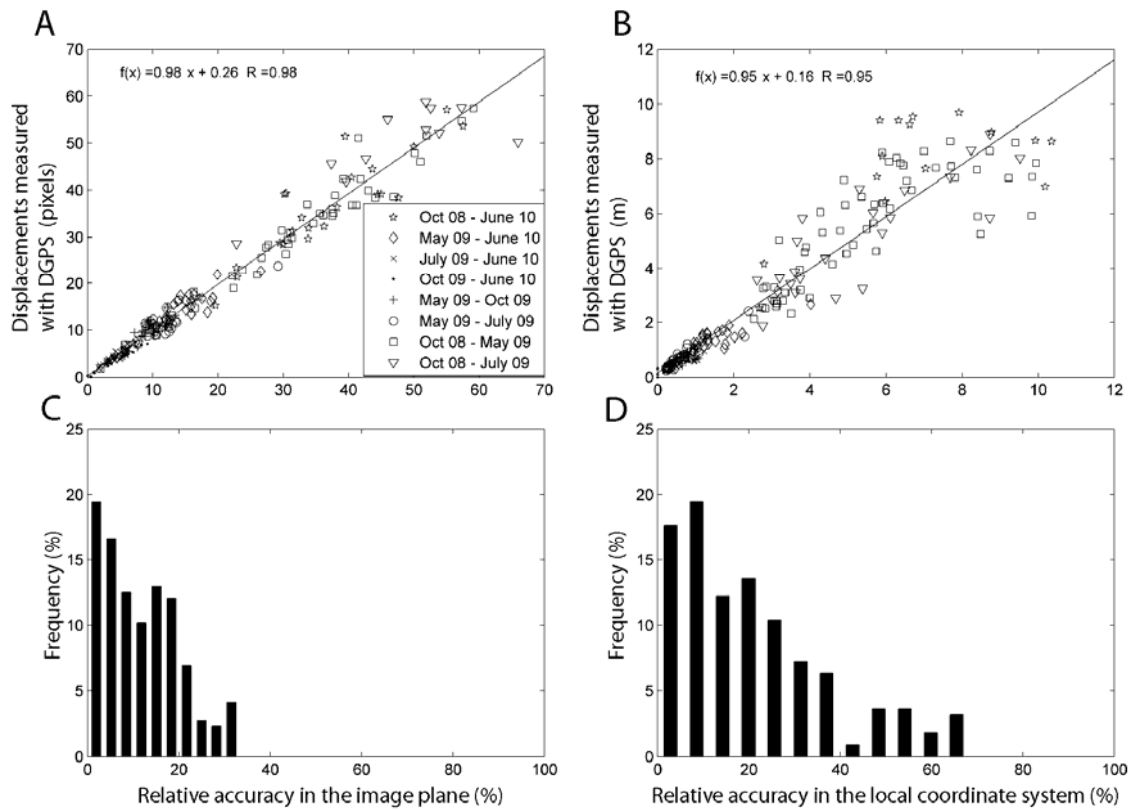


Fig. 11. Assessment of the accuracy of the Image Correlation technique. Relationships between the displacements observed by Image Correlation and the displacements observed by DGPS on sixty benchmarks in the image plane (A) and in the local coordinate system (B). Relative accuracy of the Image Correlation technique in the images plane (C) and in the local coordinate system (D).

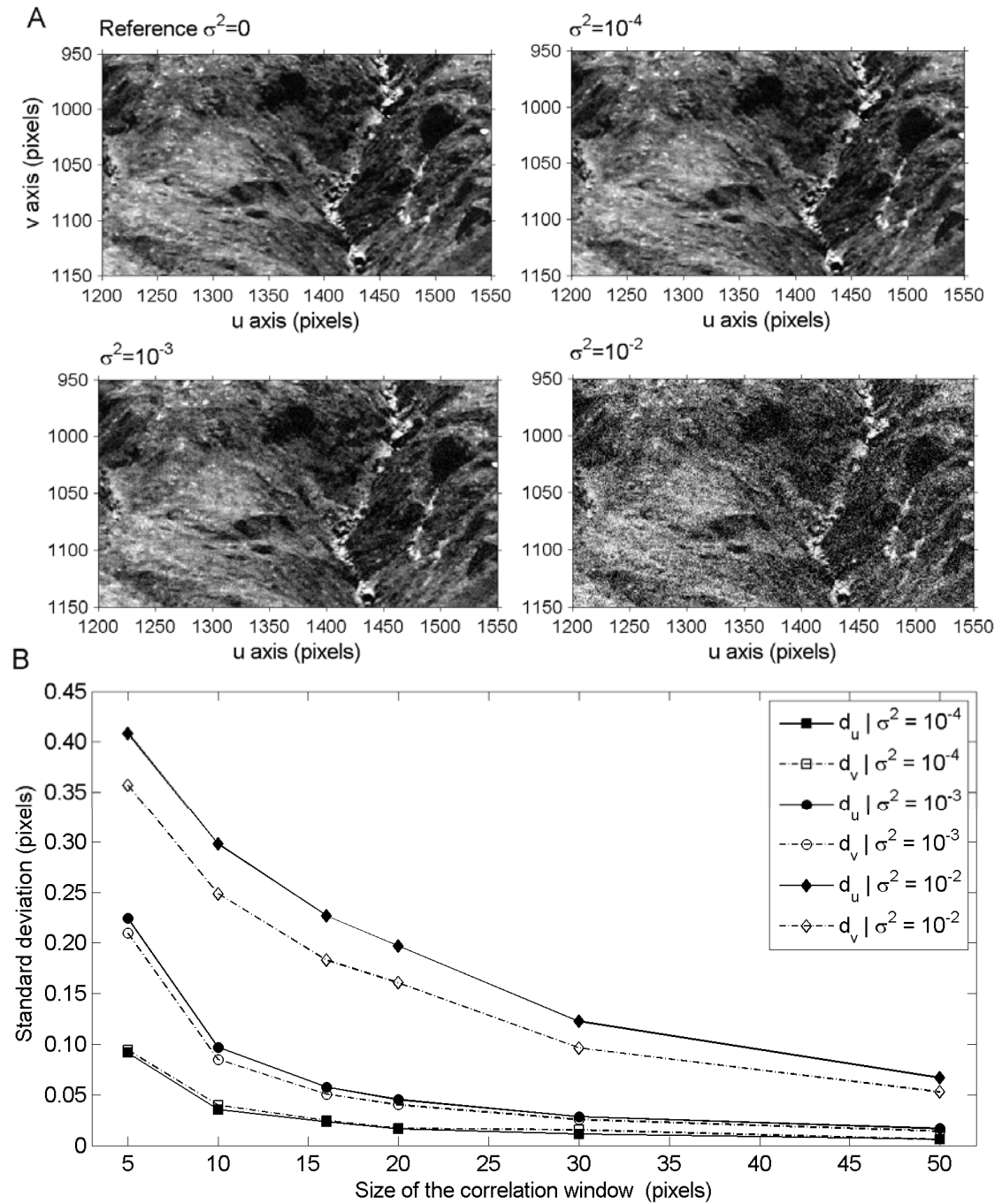


Fig. 12. Precision of the correlation algorithm. (A) Examples of different level of Gaussian noise created in the images of displacements (B) Precision of the hierarchical correlator in the  $u$  and  $v$  direction as a function of different levels of Gaussian noise ( $\sigma_n^2$ ) and different sizes of the correlation window.

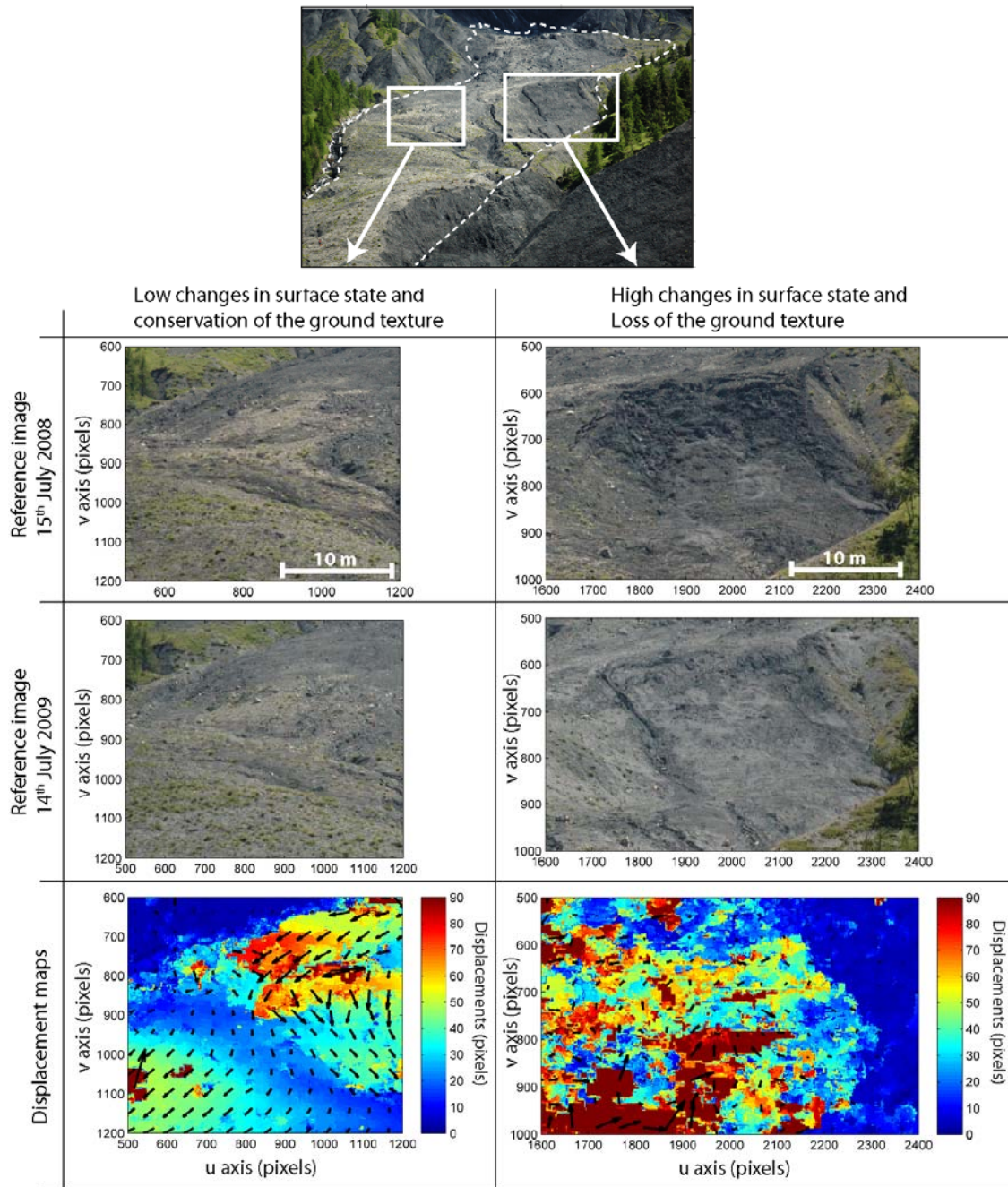


Fig. 13. Example of results for the correlation of two images acquired with one year interval (15<sup>th</sup> July 2008-14<sup>th</sup> July 2009), at the same solar time and clear sky conditions. Depending on the location in the landslide, some areas conserved their texture while others areas affected by strong weathering and ground deformation (loading of the snow and landslide displacement) display a totally different ground texture. The incoherency of the displacements is therefore clearly identifiable (inhomogeneous amplitude and direction of the displacement vectors).

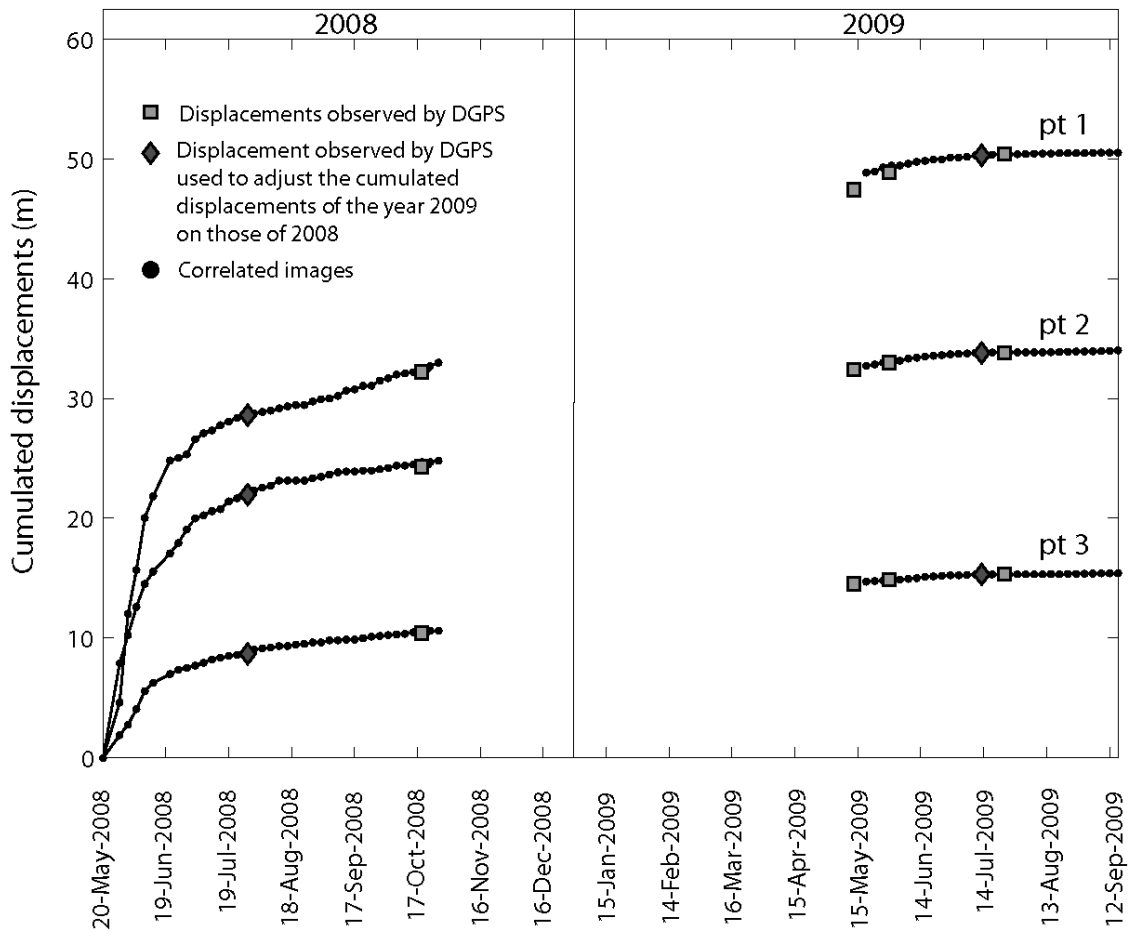


Fig. 14. Cumulated displacements at three locations in the upper (pt1), middle (pt2) and lower (pt3) parts of the landslide. The location of the points is indicated in Fig. 9. The cumulated displacements of the year 2009 are adjusted on those of 2008 using GCPs measured with DGPS at the vicinity of the points pt1, pt2 and pt3.

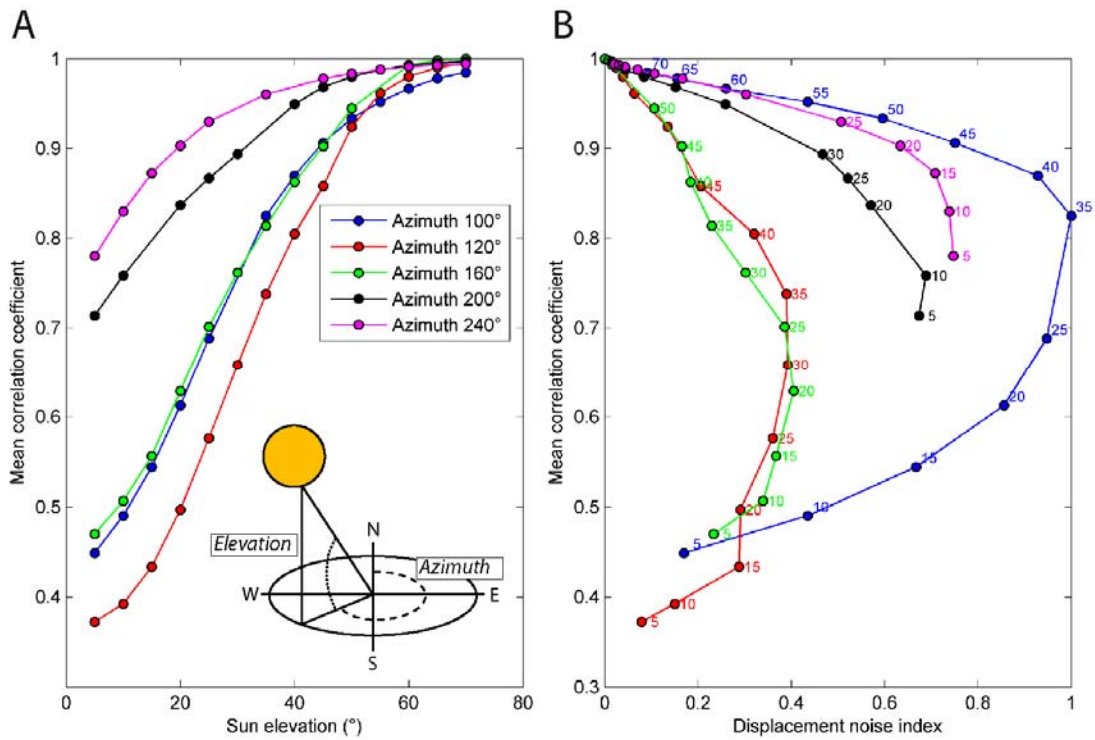


Fig. 15. Results of the correlation on the synthetic shaded relief images. (A) Influence of illumination conditions as a function of the sun elevation and azimuth on the mean correlation coefficient. (B) Relationship between displacement noise index and correlation coefficient. The values near the dots correspond to the sun elevation angles.

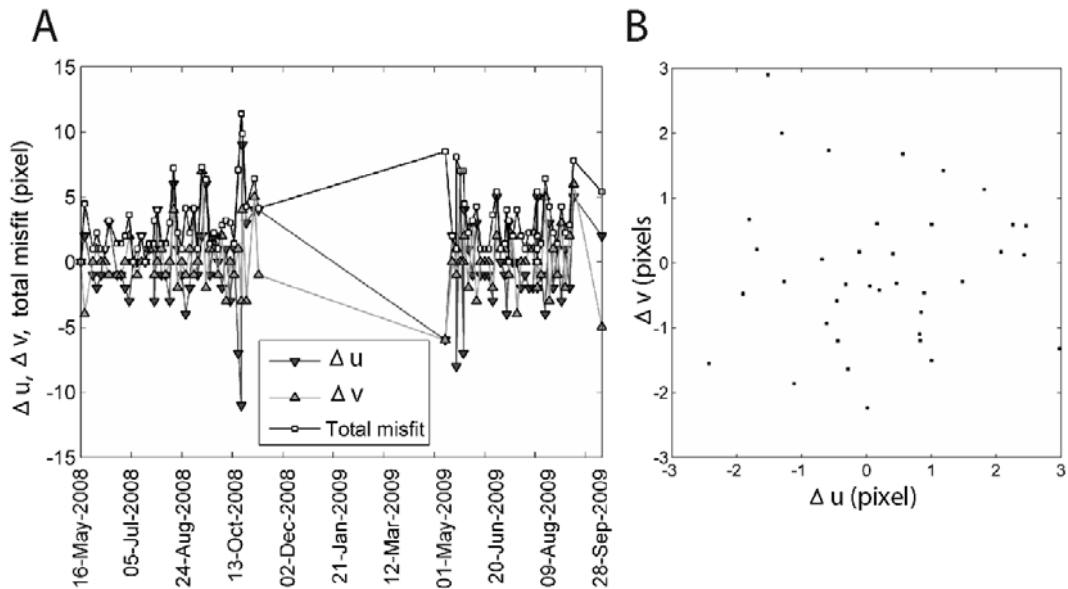


Fig. 16. Assessment of the accuracy of the camera orientation (A) Average homogenous components due to slight movement of the camera. (B) Residual  $\Delta u$  and  $\Delta v$  misfits between projected and observed GCPs after the least square minimization.

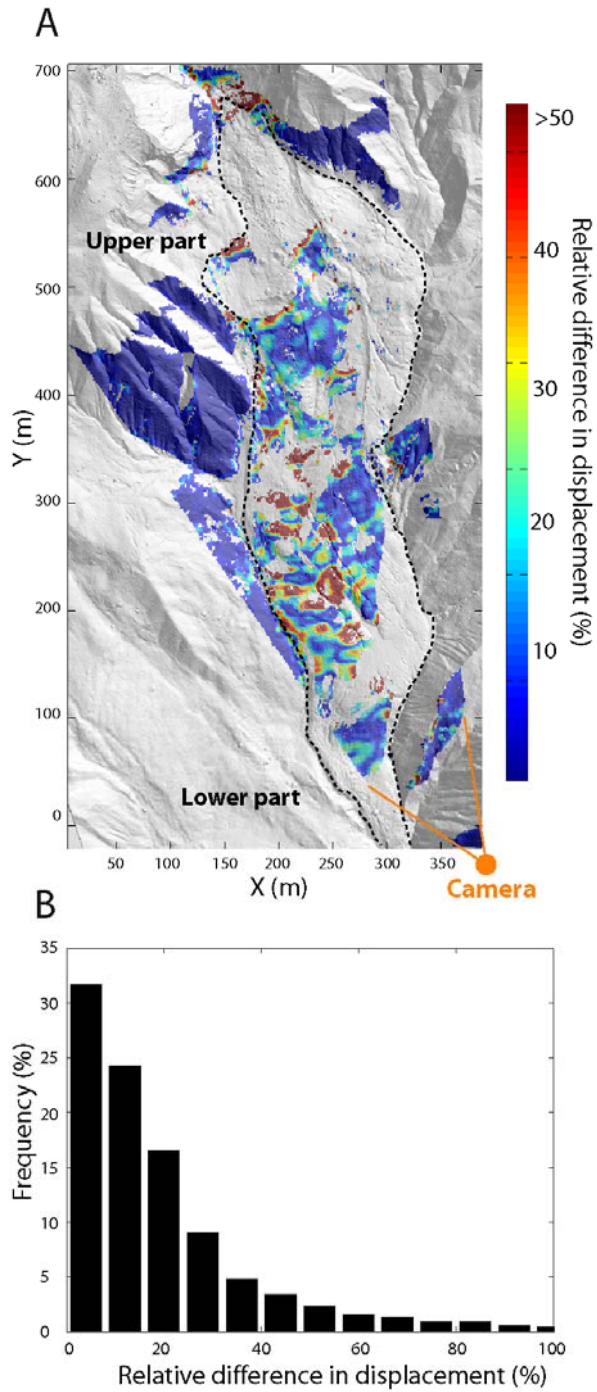


Fig. 17. Effect of the DEM on the ortho-rectification of the displacement field. (A) relative difference between the displacement field of the 1<sup>st</sup> June orthorectified with a DEM of 2007 and a DEM of 2009. (B) Histogram of the relative differences.

## Tables

Table 1. Relative advantages and disadvantages for GB-InSAR, TLS and TOP

| Techniques | Relative advantages   | Relative disadvantages  |
|------------|---|---|
| GB-InSAR   | <p>High data accuracy possible (millimetric accuracy)</p> <p>Monitoring during night and any type of weather conditions</p> <p>Atmospheric effects can be corrected (permanent scatterers)</p> <p>Potential for high level of automation in acquisition and post-processing</p>   | <p>Requires large initial investment if buying</p> <p>Skilled crew required for operation</p> <p>Displacement along line of sight</p> <p>Fails in detecting large and rapid displacements (signal decorrelation)</p> <p>Sensitive to changes in acquisition geometry and surface state variations</p>   |
| TLS        | <p>High data accuracy possible 1-4 cm (at 100 m range); 30 cm (at 1000 m range)</p> <p>Provide an easily understandable image</p> <p>Potential for high level of automation in acquisition</p>  | <p>Requires large initial investment if buying</p> <p>Skilled crew required for operation</p> <p>Computation of the true 3D displacements require specific algorithms optimized for calculations on large 3D point clouds</p> <p>Large amount of computational resources for the spatial data visualization</p> <p>Automated data post-processing difficult</p> |
| TOP        | <p>High data accuracy possible from millimeters to a few centimeters at 100 m range</p> <p>Provide an easily understandable image</p> <p>Low initial cost and operating cost</p> <p>Low energy supply (passive sensors)</p> <p>Potential for high level of automation in acquisition and post-processing</p> <p>Simple camera calibration processes available</p> <p>Simple matching algorithms available to produce DEMs and to compute 2D displacement fields</p> | <p>Adverse weather and illumination changes affects image quality</p> <p>Not operating during the night</p> <p>Very Sensitive to changes in acquisition geometry and surface state variations</p> <p>Ortho-rectification using accurate DEM is necessary for quantitative analysis</p> <p>Ground control points necessary for camera calibration</p>            |

**Table 2. Camera acquisitions characteristics**

|                  |                                   |
|------------------|-----------------------------------|
| Type of Camera   | Single-lens reflex digital camera |
| Effective Pixels | 6.1 million                       |
| Image Sensor     | RGB CCD, 23.7 x 15.6 mm           |
| Image Size       | 3008 x 2000                       |
| Sensitivity      | 400 iso                           |
| Focal length     | 52 mm                             |
| Shutter speed    | 1/800                             |
| Storage Media    | CompactFlash™ (CF) Card           |
| Storage System   | NEF (RAW)                         |

**Table 3. Quantity of interpretable displacement values in summer and in autumn after filtering according to the location in the landslide (Fig. 2)**

|                               | Total                           |                                 | 1. Correlation coefficient > 0.6 |                                 | 2. Downslope displacements      |                                 | 3. Displacements in visible areas |                                 |
|-------------------------------|---------------------------------|---------------------------------|----------------------------------|---------------------------------|---------------------------------|---------------------------------|-----------------------------------|---------------------------------|
|                               | Absolute quantity of values (-) | Relative quantity of values (%) | Absolute quantity of values (-)  | Relative quantity of values (%) | Absolute quantity of values (-) | Relative quantity of values (%) | Absolute quantity of values (-)   | Relative quantity of values (%) |
| <b>23 July - 27 July 2008</b> |                                 |                                 |                                  |                                 |                                 |                                 |                                   |                                 |
| Upper part                    | 210637                          | 100                             | 197139                           | 93.6                            | 164275                          | 78.0                            | 161221                            | 76.5                            |
| Middle part                   | 24821                           | 100                             | 23612                            | 95.1                            | 23266                           | 93.7                            | 22343                             | 90.0                            |
| Lower part                    | 61979                           | 100                             | 61255                            | 98.8                            | 59989                           | 96.8                            | 57801                             | 93.3                            |
| Whole landslide               | 297437                          | 100                             | 282006                           | 94.8                            | 247530                          | 83.2                            | 241365                            | 81.1                            |
| <b>19 Oct. - 23 Oct. 2008</b> |                                 |                                 |                                  |                                 |                                 |                                 |                                   |                                 |
| Upper part                    | 210637                          | 100                             | 183570                           | 87.2                            | 82149                           | 39.0                            | 74798                             | 35.5                            |
| Middle part                   | 24821                           | 100                             | 22847                            | 92.1                            | 20751                           | 83.6                            | 18672                             | 75.2                            |
| Lower part                    | 61979                           | 100                             | 61762                            | 99.7                            | 60019                           | 96.8                            | 57510                             | 92.8                            |
| Whole landslide               | 297437                          | 100                             | 268179                           | 90.2                            | 162919                          | 60.4                            | 150980                            | 50.8                            |

**Table 4. Mean  $\mu$  and standard deviation  $\sigma$  of the absolute accuracy for the projection in the image plane and the back-projection in the local coordinate system**

| Image plane (n=40)             | $\mu$ (pixels) | $\sigma$ (pixels) |
|--------------------------------|----------------|-------------------|
| u                              | 0.20           | 1.59              |
| v                              | -0.08          | 1.51              |
| Local coordinate system (n=11) | $\mu$ (m)      | $\sigma$ (m)      |
| X                              | 0.07           | 0.41              |
| Y                              | -0.13          | 0.53              |
| Z                              | 0.01           | 0.29              |